

# Quantum theory of light interaction with a Lorenz-Mie particle: Optical detection and three-dimensional ground-state cooling

Patrick Maurer , Carlos Gonzalez-Ballester , and Oriol Romero-Isart

*Institute for Quantum Optics and Quantum Information, Austrian Academy of Sciences, 6020 Innsbruck, Austria  
and Institute for Theoretical Physics, University of Innsbruck, 6020 Innsbruck, Austria*



(Received 13 December 2022; accepted 24 July 2023; published 26 September 2023)

We analyze theoretically the motional quantum dynamics of a levitated dielectric sphere interacting with the quantum electromagnetic field beyond the point-dipole approximation. To this end, we derive a Hamiltonian describing the fundamental coupling between photons and center-of-mass phonons, including Stokes and anti-Stokes processes, and the coupling rates for a dielectric sphere of arbitrary refractive index and size. We then derive the laser recoil heating rates and the information radiation patterns (the angular distribution of the scattered light that carries information about the center-of-mass motion) and show how to evaluate them efficiently in the presence of a focused laser beam, in either a running- or a standing-wave configuration. This information is crucial to implement active feedback cooling of optically levitated dielectric spheres beyond the point-dipole approximation. Our results predict several experimentally feasible configurations and parameter regimes where optical detection and active feedback can simultaneously cool to the ground state the three-dimensional center-of-mass motion of dielectric spheres in the micrometer regime. Scaling up the mass of the dielectric particles that can be cooled to the center-of-mass ground state is relevant not only for testing quantum mechanics at large scales but also for current experimental efforts that search for new physics (e.g., dark matter) using optically levitated sensors.

DOI: [10.1103/PhysRevA.108.033714](https://doi.org/10.1103/PhysRevA.108.033714)

## I. INTRODUCTION

The interaction of light with a dielectric sphere is not only a paradigm in optical physics [1–6] but a topic of current research in the field of levitated optomechanics [7,8]. Particularly relevant are recent experiments achieving ground-state cooling of the center-of-mass motion of an optically trapped dielectric nanosphere using either the coherent coupling to an optical resonator [9–11] or shot-noise-limited optical detection and active feedback [12–14]. These experiments have been limited to ground-state cooling of one and two center-of-mass degrees of freedom of subwavelength silica nanoparticles, that is, spheres with a radius  $R$  of around 100 nm (mass of  $10^9$  atomic mass units), thus much smaller than the optical wavelength  $\lambda_0$  of the laser light. At these scales, where  $R/\lambda_0 \ll 1$ , the electrodynamical response of the dielectric particle can be approximated by a point dipole. Within this point-dipole approximation, the understanding of how light interacts with the motion of the nanoparticle (e.g., optomechanical coupling rates, laser recoil heating rates, or information radiation patterns) [15–22] has been key to predict, optimize, and understand ground-state cooling. This theory is however rather limited and cannot be easily extended to dielectric particles for which the point-dipole approximation is not valid [23,24]. Therefore, it has hitherto remained unclear whether larger dielectric spheres with a radius comparable to or larger than the laser light wavelength can be cooled to the ground state and if so, how to achieve it.

In this article we develop a quantum electrodynamical theory of the interaction between the electromagnetic field and a

dielectric sphere of arbitrary refractive index and size. One of the main results of this theory is to show that simultaneous three-dimensional center-of-mass ground-state cooling of a dielectric sphere with a size ranging from a few hundred nanometers to several micrometers is possible using optical setups that are currently implemented in laboratories [12–14,25–28]: Shot-noise-limited optical detection of either forward- or backward-scattered light of a focused laser beam in a running- or a standing-wave configuration. Our results are thus timely and create the opportunity to bring dielectric spheres of masses ranging from  $10^9$  to  $10^{14}$  atomic mass units into the quantum regime using laser light at room temperature [29–33]. Scaling up the mass of the dielectric spheres that can be laser cooled to the ground state has applications in the search for new physics (e.g., dark matter [34–42]). In addition, in combination with nonoptical (e.g., electrostatic [43–45]) potentials, one could consider delocalizing their center of mass to scales orders of magnitude larger than their zero-point motion [46,47], thereby testing quantum mechanics at unprecedented mass scales [48–52], comparable to current and planned efforts with superconducting microspheres [53–57].

More specifically, our article contains five key results in the field of levitated optomechanics [7,8] and is organized as follows. (i) We analytically derive the optomechanical coupling rates for arbitrary dielectric spheres (Sec. II). Crucially, this is enabled by our previous work [58], where using the techniques of Ref. [59] we quantize the electromagnetic field in the presence of a nonmoving sphere in terms of normalized scattering eigenmodes. (ii) Taking the small-particle limit, we provide a rigorous justification for the phenomenological

light-matter Hamiltonian, based on the point-dipole approximation, used thus far in levitated optomechanics [15–22] (Sec. II A). (iii) We derive expressions for the recoil heating rates and the information radiation patterns [12,13,19], two core ingredients in levitated optomechanics that we define here in the context of transition amplitudes of Stokes and anti-Stokes processes, for arbitrary particle sizes, refractive indices, and an arbitrary configuration of laser fields (Sec. III). Furthermore, we simplify their expressions analytically, which enables us to evaluate them efficiently. (iv) We compute recoil heating rates and information radiation patterns in two configurations of direct experimental interest (Sec. IV), namely, a single focused Gaussian beam and two counterpropagating focused beams in a standing-wave configuration (Secs. IV B and IV C). We show results beyond the point-dipole approximation and beyond the plane-wave approximation for the illuminating beams and characterize their dependence on particle radius and numerical aperture of the focusing lens. (v) We show how the results of (iv) predict a broad parameter regime where one-, two-, and even three-dimensional center-of-mass ground-state cooling is possible for dielectric spheres ranging from a few hundred nanometers to a few micrometers (Sec. IV). In the Conclusion (Sec. V) we argue that the methods developed in this work could directly be extended to other particle shapes and degrees of freedom [60–70], thus providing a complete theoretical toolbox to describe the interaction of light with levitated dielectric objects in the quantum regime.

## II. FUNDAMENTAL HAMILTONIAN AND PHOTON-PHONON COUPLING RATES

Let us consider a dielectric sphere of radius  $R$  and mass  $M$  whose equilibrium center-of-mass position is by definition at the origin of coordinates. The center-of-mass position fluctuations around the equilibrium position are described by the quantum-mechanical position and momentum operators  $\hat{\mathbf{r}}$  and  $\hat{\mathbf{p}}$ , respectively. They fulfill the commutation relations  $[\hat{r}_\mu, \hat{p}_\nu] = i\hbar\delta_{\mu\nu}$ , where the indices  $\mu$  and  $\nu$  label the coordinate axes  $x$ ,  $y$ , and  $z$ ;  $\delta_{\mu\nu}$  is the Kronecker delta; and  $\hbar$  is the reduced Planck constant. The sphere is assumed to be in vacuum, interacting only with electromagnetic fields. We assume that the nonfluctuating part of the electromagnetic field (e.g., optical tweezer) generates a conservative potential for the center-of-mass motion given by  $V(\mathbf{r})$ . We model the electromagnetic response of the dielectric sphere as homogeneous, isotropic, and lossless. We assume that the dielectric sphere interacts significantly only with electromagnetic field modes in a sufficiently narrow frequency window so that its electromagnetic response can be described by a single scalar and real relative permittivity  $\epsilon$ . Assuming sufficiently small center-of-mass displacements, that is,  $\Delta r_\mu \equiv \langle \hat{r}_\mu^2 - \langle \hat{r}_\mu \rangle^2 \rangle^{1/2}$  smaller than any relevant length scale associated with the electromagnetic fields, the total Hamiltonian describing the interaction between the center-of-mass motion and the electromagnetic field can be expressed as

$$\hat{H} = \frac{\hat{\mathbf{p}}^2}{2M} + V(\hat{\mathbf{r}}) + \hat{H}_{\text{em}} - \hat{\mathcal{F}} \cdot \hat{\mathbf{r}}. \quad (1)$$

Here  $\hat{H}_{\text{em}}$  describes the free dynamics of the electromagnetic field in the presence of a fixed dielectric sphere at the origin of coordinates, the derivation and thorough discussion of which are the focus of our previous work [58]. The last term, which is the focus of this article, describes the interaction of the electromagnetic field with the center-of-mass position. Note that the small-displacement assumption manifests in an interaction term that is linear in the position operators and depends on the specific form of the operator  $\hat{\mathcal{F}}$ , which hereafter we call the *radiation pressure operator*. As we show below,  $\hat{\mathcal{F}}$  depends on the electromagnetic field degrees of freedom, is nonlinear with the electromagnetic fields, and does not commute with  $\hat{H}_{\text{em}}$ , namely,  $[\hat{H}_{\text{em}}, \hat{\mathcal{F}}_\mu] \neq 0$  for any  $\mu$ . We remark that by definition of  $V(\mathbf{r})$  we have that

$$\nabla V(\mathbf{r})|_{\mathbf{r}=0} = \langle \hat{\mathcal{F}} \rangle. \quad (2)$$

Here  $\langle \hat{\mathcal{F}} \rangle$  represents the quantum-mechanical expected value of  $\hat{\mathcal{F}}$  for a given state of the electromagnetic field and the time average over the relevant timescale of the electromagnetic field. The relevant electromagnetic timescale (e.g., optical time period) is assumed to be much shorter than the mechanical timescales associated with the motion of the dielectric sphere. In the context of discussing center-of-mass cooling, we will consider the potential  $V(\mathbf{r})$  to be a standard three-dimensional anisotropic harmonic potential with harmonic frequencies  $\Omega_\mu$ , namely,

$$V(\hat{\mathbf{r}}) = \frac{M}{2} \sum_\mu \Omega_\mu^2 \hat{r}_\mu^2. \quad (3)$$

We write position and momentum operators in terms of bosonic creation  $\hat{b}_\mu^\dagger$  and annihilation  $\hat{b}_\mu$  operators, namely,  $\hat{r}_\mu = r_{0\mu}(\hat{b}_\mu^\dagger + \hat{b}_\mu)$  and  $\hat{p}_\mu = iM\Omega_\mu r_{0\mu}(\hat{b}_\mu^\dagger - \hat{b}_\mu)$ , where  $r_{0\mu} \equiv [\hbar/(2M\Omega_\mu)]^{1/2}$  is the zero-point motion and  $[\hat{b}_\mu, \hat{b}_\nu^\dagger] = \delta_{\mu\nu}$ .

Let us now discuss the specific form of the radiation pressure operator  $\hat{\mathcal{F}}$ . Using Eq. (1), we can show that the Heisenberg equation of motion for the  $\mu$  component of the center-of-mass position operator of the dielectric sphere is given by

$$\frac{d^2 \hat{r}_\mu}{dt^2} + \Omega_\mu^2 \hat{r}_\mu = \frac{\hat{\mathcal{F}}_\mu}{M}. \quad (4)$$

We obtain an expression for the radiation pressure operator by deriving the equivalent classical equation of motion according to electrodynamics in the presence of a dielectric object, promoting the dynamical variables (position, momentum, and electromagnetic fields) to quantum operators, and comparing the resulting equation with Eq. (4). The right-hand side of such an equation is the radiation pressure exerted by the self-consistent electromagnetic fields, which in electrodynamics can be expressed by a surface integral of the Maxwell stress tensor in the far field of the dielectric sphere [71,72]. Based on this, we define the vector component of the radiation pressure operator  $\hat{\mathcal{F}}_\mu$ , written in terms of the electric field  $\hat{\mathbf{E}}(\mathbf{r})$  and magnetic field  $\hat{\mathbf{B}}(\mathbf{r})$  operators, as

$$\hat{\mathcal{F}}_\mu \equiv -\frac{\epsilon_0}{2} \lim_{r \rightarrow \infty} r^2 \int d\Omega (\mathbf{e}_r \cdot \mathbf{e}_\mu) [\hat{\mathbf{E}}^2(\mathbf{r}) + c^2 \hat{\mathbf{B}}^2(\mathbf{r})]. \quad (5)$$

Here  $r = |\mathbf{r}|$ ,  $d\Omega$  is the surface element in spherical coordinates,  $\mathbf{e}_r$  is the radial unit vector,  $\mathbf{e}_\mu$  is the  $\mu$ -axis unit vector, and  $\epsilon_0$  and  $c$  are the permittivity and speed of light in vacuum. The expression (5) fully determines the fundamental Hamiltonian in Eq. (1) describing the interaction of light with the center-of-mass motion of a dielectric sphere of arbitrary refractive index and size in the small-displacement regime.

Let us now expand the electric and magnetic field operators in terms of the normalized eigenmodes for a fixed sphere at the origin of coordinates, namely,

$$\hat{\mathbf{E}}(\mathbf{r}) = i \sum_{\kappa} \sqrt{\frac{\hbar\omega_{\kappa}}{2\epsilon_0}} [\mathbf{F}_{\kappa}(\mathbf{r}) \hat{a}_{\kappa} - \text{H.c.}], \quad (6)$$

$$\hat{\mathbf{B}}(\mathbf{r}) = \sum_{\kappa} \sqrt{\frac{\hbar}{2\epsilon_0\omega_{\kappa}}} [\nabla \times \mathbf{F}_{\kappa}(\mathbf{r}) \hat{a}_{\kappa} + \text{H.c.}] \quad (7)$$

Here we denote by  $\mathbf{F}_{\kappa}(\mathbf{r})$  the normalized scattering eigenmodes in the presence of a nonmoving dielectric sphere, whose calculation and quantization for arbitrary particle sizes and refractive indices were the object of our previous work [58]. The normalized scattering eigenmodes are defined by the multi-index  $\kappa = (g, \mathbf{k})$ , where  $g = 1, 2$  is a polarization index with associated polarization unit vector  $\mathbf{e}_g$  and  $\mathbf{k} \in \mathbb{R}^3$  is the wave vector. They are composed of a plane-wave contribution with mode index  $\kappa$  (i.e., wave vector  $\mathbf{k}$  and transverse polarization vector  $\mathbf{e}_g$ ) and a scattered contribution describing the elastic scattering of the plane-wave component off the dielectric sphere. In essence, they are properly normalized solutions of the Lorenz-Mie problem [1,2], which allow us to fully include all the elastic scattering processes (i.e., the scattering of light by the nonmoving dielectric particle) exactly. The mode frequency is given by  $\omega_{\kappa} = c|\mathbf{k}|$ . The associated creation and annihilation operators fulfill the bosonic commutation rules  $[\hat{a}_{\kappa}, \hat{a}_{\kappa'}^\dagger] = \delta_{\kappa\kappa'}$ .<sup>1</sup> In terms of the normalized eigenmodes, the Hamiltonian  $\hat{H}_{\text{em}}$  describing the free dynamics of the electromagnetic field for a fixed sphere is diagonal, namely,  $\hat{H}_{\text{em}} = \sum_{\kappa} \hbar\omega_{\kappa} \hat{a}_{\kappa}^\dagger \hat{a}_{\kappa}$ , for spheres of all refractive indices and sizes [58]. The expansion in terms of normalized scattering eigenmodes is a crucial step to obtain exact analytical expressions of quantities of interest and is in contrast to the usual field expansion in terms of, e.g., plane waves, for which the Hamiltonian is not diagonal. Such cases require the use of approximative expansions which fail for large enough particles [23].

We can now express the Hamiltonian (1) in terms of bosonic creation and annihilation operators only, resulting in a Hamiltonian that describes the dynamics of photons interacting with center-of-mass phonons. Hereafter, we refer to a photon as the excitation of an eigenmode of the electromagnetic field in the presence of the dielectric sphere at equilibrium. This Hamiltonian is obtained by introducing

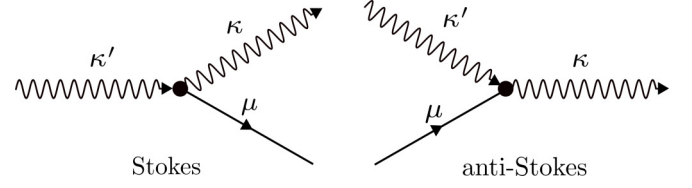


FIG. 1. Feynman diagrams of the two fundamental interaction processes as described by the third term in Eq. (8). Photons in mode  $\kappa'$  are inelastically scattered at a coupling rate  $g_{\kappa\kappa'\mu}$  into mode  $\kappa$  through generation (Stokes) or absorption (anti-Stokes) of a phonon in mode  $\mu$ .

Eqs. (6) and (7) into Eq. (5) and performing a rotating-wave approximation that neglects all rapidly oscillating terms. The rotating-wave approximation is valid in the standard weak-coupling regime where the bare photon-phonon interaction coupling rate is smaller than the phonon frequencies.<sup>2</sup> The Hamiltonian (1) can then be written as

$$\begin{aligned} \hat{H} = & \sum_{\mu} \hbar\Omega_{\mu} \hat{b}_{\mu}^\dagger \hat{b}_{\mu} + \sum_{\kappa} \hbar\omega_{\kappa} \hat{a}_{\kappa}^\dagger \hat{a}_{\kappa} \\ & + \hbar \sum_{\kappa\kappa'\mu} g_{\kappa\kappa'\mu} \hat{a}_{\kappa}^\dagger \hat{a}_{\kappa'} (\hat{b}_{\mu}^\dagger + \hat{b}_{\mu}). \end{aligned} \quad (8)$$

The third term describes the two fundamental processes describing the interaction of light and center-of-mass motion as illustrated in Fig. 1, that is, (i) Stokes processes, in which a photon in mode  $\kappa'$  is inelastically scattered into a photon of lower frequency in mode  $\kappa$  by generating a phonon in mode  $\mu$ , and (ii) anti-Stokes processes, in which a photon in mode  $\kappa'$  is inelastically scattered into a photon of higher frequency in mode  $\kappa$  by absorbing a phonon in mode  $\mu$ .

The physics of the photon-phonon interaction is encoded in the coupling rates  $g_{\kappa\kappa'\mu}$  of Eq. (8), which can be written as

$$\begin{aligned} g_{\kappa\kappa'\mu} = & r_{0\mu} \frac{c\sqrt{kk'}}{2} \lim_{r \rightarrow \infty} r^2 \int d\Omega (\mathbf{e}_r \cdot \mathbf{e}_{\mu}) \\ & \times \left( \mathbf{F}_{\kappa}^*(\mathbf{r}) \cdot \mathbf{F}_{\kappa'}(\mathbf{r}) + \frac{1}{kk'} \nabla \times \mathbf{F}_{\kappa}^*(\mathbf{r}) \cdot \nabla \times \mathbf{F}_{\kappa'}(\mathbf{r}) \right), \end{aligned} \quad (9)$$

with  $k = |\mathbf{k}|$ . Specifically, they correspond to a surface integral in the far field of a function that depends on the normalized scattering eigenmodes [58]. As shown in Appendix A 1, the far-field expression of the scattering modes can be written in terms of vector spherical harmonics with angular momentum mode indices  $l = 1, 2, \dots$  and  $m = -l, -l+1, \dots, l$ , which can be mapped to the angular distribution of the electromagnetic fields radiated by electric and magnetic multipoles. The angular integrals (9), containing products of vector spherical harmonics, can be analytically performed using the results of [73]. This means that the couplings  $g_{\kappa\kappa'\mu}$  for a dielectric sphere of arbitrary refractive index

<sup>1</sup>We remark that throughout the article we use the notation wherein sums over a multi-index  $\kappa$  must be understood as integrals over continuous indices and sums over discrete ones, namely,  $\sum_{\kappa} \equiv \int d\mathbf{k} \sum_g$ . A Kronecker delta of a multi-index must be understood as a product of Dirac deltas for the continuous indices and Kronecker deltas for discrete indices, namely,  $\delta_{\kappa\kappa'} \equiv \delta(\mathbf{k} - \mathbf{k}')\delta_{gg'}$ .

<sup>2</sup>Note that the rotating-wave approximation also requires the frequencies of the electromagnetic field to be large compared to the phonon frequencies. This condition is satisfied for the narrowband and high-frequency optical modes considered in this work.

and size can be analytically expressed as a sum over discrete angular momentum and polarization indices that can be efficiently evaluated [see Eq. (A19)]. This is one of the main results of this article. Let us remark that we have explicitly confirmed that the Hamiltonian (8) with the coupling rates (9) can also be obtained applying perturbation theory to the electromagnetic Hamiltonian, as described in [74,75] in the context of Brillouin scattering in photonic waveguides.

### A. Coupling rates in the small-particle limit

As a consistency check, one can show (details in Appendix A 1) that in the small-particle limit  $\sqrt{\epsilon}kR \rightarrow 0$ , the lowest-order term of the photon-phonon coupling rates (9) can be written as

$$g_{\kappa\kappa'\mu} \simeq \frac{i r_{0\mu} \alpha}{\epsilon_0} \frac{c k k'}{2(2\pi)^3} (\mathbf{e}_g^* \cdot \mathbf{e}_{g'}) (\mathbf{e}_k - \mathbf{e}_{k'}) \cdot \mathbf{e}_\mu, \quad (10)$$

where  $\alpha = 3\epsilon_0 V(\epsilon - 1)/(\epsilon + 2)$  is the polarizability of the dielectric sphere,  $V$  denotes the volume of the sphere, and  $\mathbf{e}_k$  denotes the unit vector parallel to the wave vector  $\mathbf{k}$ . The consistently derived small-particle coupling rates (10) agree with the coupling rates used in the current literature [15–18,20–23], where they are heuristically derived by making a Taylor expansion of the interacting Hamiltonian  $-\alpha\hat{\mathbf{E}}^2(\hat{\mathbf{r}})/2$  with the electric field operator expanded in plane-wave modes (point-dipole approximation). The latter can be obtained by replacing the scattering normalized modes  $\mathbf{F}_\kappa(\mathbf{r})$  in Eq. (6) by plane-wave modes  $\mathbf{G}_\kappa(\mathbf{r}) \equiv \exp(i\mathbf{k} \cdot \mathbf{r}) \mathbf{e}_g (2\pi)^{-3/2}$ . We find this agreement an important result from a theoretical point of view, as it provides a sound justification of the interacting Hamiltonian  $-\alpha\hat{\mathbf{E}}^2(\hat{\mathbf{r}})/2$  used to describe the interaction of light with a small dielectric particle in the quantum regime. Furthermore, the comparison of Eq. (10) with Eq. (9) provides a clear route to make predictions that go beyond the point-dipole approximation and that could be observed in current experiments, as we show in the rest of the article.

### B. Linearized Hamiltonian in the presence of a classical field

Let us consider the scenario where some of the electromagnetic field modes are in a coherent state, that is, the quantum state of the electromagnetic field in the presence of the non-moving sphere at the origin is given by

$$|\Psi_{\text{cl}}\rangle = \exp\left(\sum_\kappa (\alpha_\kappa \hat{a}_\kappa^\dagger - \alpha_\kappa^* \hat{a}_\kappa)\right) |0\rangle. \quad (11)$$

Here  $\alpha_\kappa$  is the coherent complex amplitude of the mode  $\kappa$ , that is,  $\hat{a}_\kappa |\Psi_{\text{cl}}\rangle = \alpha_\kappa |\Psi_{\text{cl}}\rangle$ . The distribution in  $\kappa$  of  $\alpha_\kappa$  specifies the particular state of the electromagnetic field. The classical electromagnetic field associated with this coherent quantum state is given by

$$\begin{aligned} \mathbf{E}_{\text{cl}}(\mathbf{r}, t) &\equiv \langle \Psi_{\text{cl}} | \hat{\mathbf{E}}(\mathbf{r}, t) | \Psi_{\text{cl}} \rangle \\ &= i \sum_\kappa \sqrt{\frac{\hbar\omega_\kappa}{2\epsilon_0}} [\mathbf{F}_\kappa(\mathbf{r}) \alpha_\kappa e^{-i\omega_\kappa t} - \text{c.c.}] \end{aligned} \quad (12)$$

Since in most of the experiments in levitated optomechanics the classical electromagnetic field is generated by a quasi-monochromatic laser light, hereafter we will assume that all

the modes found in this coherent state have the same frequency, labeled by  $\omega_0$ . As it is common in optomechanics, we can now derive the linearized Hamiltonian describing the dynamics of the fluctuations of the electromagnetic field above  $|\Psi_{\text{cl}}\rangle$  caused by their interaction with the center-of-mass motion of the dielectric sphere. In a rotating frame with frequency  $\omega_0$ , this linearized Hamiltonian is given by

$$\begin{aligned} \hat{H}_{\text{lin}} &= \sum_\kappa \hbar \Delta_\kappa \hat{a}_\kappa^\dagger \hat{a}_\kappa + \sum_\mu \hbar \Omega_\mu \hat{b}_\mu^\dagger \hat{b}_\mu \\ &+ \hbar \sum_{\kappa\mu} (G_{\kappa\mu} \hat{a}_\kappa^\dagger + G_{\kappa\mu}^* \hat{a}_\kappa) (\hat{b}_\mu^\dagger + \hat{b}_\mu), \end{aligned} \quad (13)$$

where we have defined the detuning  $\Delta_\kappa \equiv \omega_\kappa - \omega_0$  for each mode and the linearized coupling rate

$$G_{\kappa\mu} \equiv \sum_{\kappa'} \alpha_{\kappa'} g_{\kappa\kappa'\mu}. \quad (14)$$

We remark that the potential describing the center-of-mass motion in the presence of the electromagnetic field  $|\Psi_{\text{cl}}\rangle$  is defined so that Eq. (2) is fulfilled, that is, it includes the radiation pressure exerted by the classical electromagnetic field. Indeed, in most cases the classical electromagnetic field  $\mathbf{E}_{\text{cl}}(\mathbf{r}, t)$  represents the field used for optical trapping.

As we show in the next section, the fundamental coupling rates  $g_{\kappa\kappa'\mu}$  [Eq. (9)] and the distribution of coherent amplitudes  $\alpha_\kappa$  for a given classical electromagnetic field [Eq. (11)] are the key ingredients to analyze the quantum dynamics of a trapped dielectric sphere interacting with light.

## III. RECOIL HEATING RATES AND INFORMATION RADIATION PATTERNS

As shown in the preceding section, the fundamental transitions occurring during the interaction of light with a trapped particle are given by Stokes and anti-Stokes processes (see Fig. 1). These are the only processes that change the center-of-mass state of the particle. In the presence of a highly excited electromagnetic field, such as the classical electromagnetic field given by  $|\Psi_{\text{cl}}\rangle$  [Eq. (11)], Stokes and anti-Stokes processes are significant, and the overall effective dynamics is described by the linearized Hamiltonian (13). These effective dynamics yield two important phenomena: (i) dissipative center-of-mass dynamics, namely, laser light recoil heating, and (ii) the scattering of light carrying information about the center-of-mass position fluctuations, the angular distribution of which is called the information radiation pattern (IRP).

To better define and evaluate these two quantities, let us consider the transition amplitude for the Stokes and anti-Stokes process in the presence of a classical electromagnetic field. The transition amplitudes associated with these processes can be evaluated as [76]

$$\tau_{\kappa\mu}^p \equiv \langle \Psi_{\text{out}}^p | \hat{U}(T/2, -T/2) | \Psi_{\text{in}} \rangle. \quad (15)$$

Here the input state is given by  $|\Psi_{\text{in}}\rangle \equiv |n_x, n_y, n_z\rangle \otimes |\Psi_{\text{cl}}\rangle$ , where  $|n_x, n_y, n_z\rangle$  ( $n_\mu > 0$ ) is a product Fock state for the three center-of-mass degrees of freedom and the quantum state of the electromagnetic field is given by  $|\Psi_{\text{cl}}\rangle = \mathcal{D}(\alpha_\kappa) |0\rangle_{\text{em}}$ , as defined in Eq. (11), with the monochromatic coherent amplitude  $\alpha_\kappa$  with frequency  $\omega_0$ . The output state is given

by  $|\Psi_{\text{out}}^S\rangle \equiv \hat{a}_\kappa^\dagger \hat{b}_\mu^\dagger |\Psi_{\text{in}}\rangle$  and  $|\Psi_{\text{out}}^{\text{aS}}\rangle \equiv \hat{a}_\kappa^\dagger \hat{b}_\mu |\Psi_{\text{in}}\rangle$  for the Stokes ( $p = S$ ) and anti-Stokes ( $p = \text{aS}$ ) transitions, respectively. The time-evolution operator in the Schrödinger picture is given by  $\hat{U}(t, t') = \exp[-i\hat{H}(t - t')/\hbar]$ , where  $\hat{H}$  is our fundamental Hamiltonian (8). We emphasize that for  $\tau_{\kappa\mu}^p$  to be nonzero, the incoming photon in the Stokes or anti-Stokes transition, namely, the photon in mode  $\kappa'$  according to Fig. 1, has to be in a mode excited by the classical electromagnetic field, whereas the Stokes or anti-Stokes scattered photon in mode  $\kappa$  can be in any of the available electromagnetic field modes, i.e., vacuum state or any mode excited by the electromagnetic field.

A quantity of interest in this context is the transition probability rate in the asymptotic limit [76] of the Stokes and anti-Stokes processes integrated over all  $\kappa$ , namely,  $\lim_{T \rightarrow \infty} \sum_\kappa |\tau_{\kappa\mu}^p|^2 / T$ . As we show in Appendix A 2, the transition probability rates can be evaluated using first-order perturbation theory (i.e., Fermi's golden rule) and lead to

$$\lim_{T \rightarrow \infty} \frac{\sum_\kappa |\tau_{\kappa\mu}^S|^2}{T} = (n_\mu + 1) \Gamma_\mu^+, \quad (16)$$

$$\lim_{T \rightarrow \infty} \frac{\sum_\kappa |\tau_{\kappa\mu}^{\text{aS}}|^2}{T} = n_\mu \Gamma_\mu^-, \quad (17)$$

where

$$\Gamma_\mu^\pm \equiv 2\pi \sum_\kappa |G_{\kappa\mu}|^2 \delta(\omega_\kappa - \omega_0 \pm \Omega_\mu). \quad (18)$$

The linearized couplings in free space are broadband over a frequency window given by  $\Omega_\mu$ , i.e., they fulfill  $|\Gamma_\mu^+ - \Gamma_\mu^-| \ll \Gamma_\mu^+ + \Gamma_\mu^-$ , and hence we define the transition probability rate

$$\Gamma_\mu = 2\pi \sum_\kappa |G_{\kappa\mu}|^2 \delta(\omega_\kappa - \omega_0), \quad (19)$$

that is,  $\Gamma_\mu \approx \Gamma_\mu^+ \approx \Gamma_\mu^-$  in the broad coupling regime. In this regime we can show using standard techniques in open quantum system dynamics (e.g., Langevin equations and Born-Markov master equation) that the reduced motional dynamics described by the fundamental Hamiltonian (8) leads to

$$\frac{d}{dt} \langle \hat{b}_\mu^\dagger \hat{b}_\mu \rangle(t) = \Gamma_\mu, \quad (20)$$

that is, center-of-mass recoil heating with a phonon heating rate given by  $\Gamma_\mu$  [77]. Let us emphasize that when the particle is not in free space but in environments that change the mode structure of the electromagnetic field (e.g., a particle inside an optical resonator), the system is not in the broadband coupling regime, leading to  $\Gamma_\mu^+ \neq \Gamma_\mu^-$ , and hence to the possibility of passively cooling the center-of-mass motion of the particle [9–11,20,78,79].

The photons scattered via a Stokes or anti-Stokes process carry information about the center-of-mass motion, that is, they are entangled with the center-of-mass motional degrees of freedom. The knowledge of where they scatter, namely, their angular probability distribution, is key to collect them, measure them, and process the information to exert active feedback to the particle. This knowledge is provided by the (IRP)  $\mathcal{I}_\mu^p(\theta_k, \phi_k)$  associated to the center-of-mass motion along the  $\mu$  axis, which is defined as the normalized angular

distribution of the transition probability rate in the asymptotic limit, namely,

$$\mathcal{I}_\mu^p(\theta_k, \phi_k) \equiv \frac{\lim_{T \rightarrow \infty} \int_0^\infty dk k^2 \sum_g |\tau_{\kappa\mu}^p|^2}{\lim_{T \rightarrow \infty} \sum_\kappa |\tau_{\kappa\mu}^p|^2}. \quad (21)$$

Note that, by definition,  $\int d\theta_k d\phi_k \sin \theta_k \mathcal{I}_\mu^p(\theta_k, \phi_k) = 1$ . The IRP  $\mathcal{I}_\mu^p(\theta_k, \phi_k)$  provides the solid-angle probability distribution of a photon scattered through either a Stokes or an anti-Stokes process. Within the broadband coupling regime, we obtain that

$$\mathcal{I}_\mu(\theta_k, \phi_k) = \frac{\sum_g \int_0^\infty dk k^2 |G_{\kappa\mu}|^2 \delta(\omega_\kappa - \omega_0)}{\sum_\kappa |G_{\kappa\mu}|^2 \delta(\omega_\kappa - \omega_0)}. \quad (22)$$

In this regime, the IRP is the same for a Stokes and an anti-Stokes process, showing that these processes can be distinguished by measuring the frequency of the scattered photon but not by its angular probability distribution.

Both the laser recoil heating rate  $\Gamma_\mu$  and the IRP  $\mathcal{I}_\mu(\theta_k, \phi_k)$  are fully determined by the linearized coupling rate  $G_{\kappa\mu}$ , that is, by the coupling rates  $g_{\kappa\kappa'\mu}$  [Eq. (9)] and the coherent amplitude  $\alpha_\kappa$  associated with a given classical electromagnetic field [Eq. (11)]. In Appendix A 3 we show how Eqs. (19) and (22) can be expressed in an explicit form as a sum over discrete angular momentum and polarization indices [see Eqs. (A44) and (A46)], which makes their evaluation numerically efficient. Hence, our theory allows us to efficiently evaluate recoil heating rates and IRPs for spheres of arbitrary refractive index and size and in the presence of arbitrary combinations of electromagnetic field modes in a coherent state. This is one of the main results of this article.

The knowledge of the laser recoil heating rate  $\Gamma_\mu$  and the IRP  $\mathcal{I}_\mu(\theta_k, \phi_k)$  is crucial to implement active feedback cooling via optical detection [12–14,25,26]. In particular, the minimum achievable mean phonon-occupation number reads [12,13,19]

$$\bar{n}_\mu \equiv \frac{1}{2} \left( \frac{1}{\sqrt{\eta_\mu}} - 1 \right). \quad (23)$$

Here  $\eta_\mu \equiv \eta_\mu^d \eta_\mu^e \eta_\mu^o$  denotes the total efficiency and is determined by (i) the detection efficiency

$$\eta_\mu^d \equiv \int_{S_d} d\theta_k d\phi_k \sin \theta_k \mathcal{I}_\mu(\theta_k, \phi_k), \quad (24)$$

where  $S_d$  denotes the solid angle that is covered by the collection lens; (ii) the efficiency associated with environmental information loss

$$\eta_\mu^e \equiv \frac{\Gamma_\mu}{\Gamma_\mu + \Gamma_\mu^g}, \quad (25)$$

where the heating rate  $\Gamma_\mu^g$  due to environmental gas at pressure  $p$  and temperature  $T$  is given by

$$\Gamma_\mu^g = 0.619 \frac{r_{0\mu}^2 p}{\hbar^2} 6\pi R^2 \sqrt{\frac{8k_B T m_0}{\pi}}, \quad (26)$$

where  $m_0$  denotes the molecular mass of the environmental gas and  $k_B$  is the Boltzmann constant [30,80] note that we are assuming that other sources of environmental noise,

e.g., displacement noise in the trapping potential, center-of-mass coupling to internal acoustic phonons, and emission of blackbody radiation, are negligible, namely, their associated heating rates are smaller than  $\Gamma_\mu + \Gamma_g$ ; and (iii) the efficiency  $\eta_\mu^o$  associated with all other information loss channels in the active feedback scheme, e.g., mode matching, detector noise, and digital noise [12,13]. Hereafter, we consider ideal feedback, i.e.,  $\eta_\mu^o = 1$ .

Equation (23) shows that a necessary condition to achieve center-of-mass ground-state cooling along the  $\mu$  axis, defined as  $\bar{n}_\mu < 1$ , is  $\eta_\mu > \frac{1}{9} \approx 0.11$ . We emphasize that our analysis will be particularly relevant in experimental situations where center-of-mass heating rates are dominated by  $\Gamma_\mu + \Gamma_g$  and for nearly ideal feedback schemes with  $\eta_\mu^o \lesssim 1$ . Finally, we remark that with particles beyond the point-dipole approximation, recoil heating rates will be typically comparable to or even larger than the mechanical frequencies, which will require fast feedback schemes optimized to operate in these regimes.

In the following section we will explicitly show how this theory can be applied to study a case which is very relevant to current experimental efforts [12–14,25–28]: A dielectric silica sphere of arbitrary refractive index and size interacting with a focused monochromatic laser, in either a running- or a standing-wave configuration. Our analysis will show in which regimes center-of-mass ground-state cooling of a sphere could be achieved via active feedback cooling, that is, in which regimes  $\eta_\mu^d \eta_\mu^e > \frac{1}{9}$  and hence  $\bar{n}_\mu < 1$ . Remarkably, we will predict several experimentally feasible configurations in which simultaneous three-dimensional (3D) ground-state cooling via active feedback is possible.

#### IV. CASE STUDY

Let us apply the theoretical methods developed in this article to study a case that is of relevance to current experimental efforts. In particular, we will evaluate the recoil heating rates  $\Gamma_\mu$  and the information radiation patterns  $\mathcal{I}_\mu(\theta_k, \phi_k)$  for a trapped dielectric sphere made of silica interacting with a focused laser beam, either in a running-wave configuration or in a standing-wave configuration (see Fig. 2). In both cases the equilibrium position of the dielectric sphere is assumed to be at the focus. In the standing-wave configuration, we will include a relative phase  $\Phi$  between the two counterpropagating beams so that at focus one can have an intensity maximum ( $\Phi = 0$ ), an intensity gradient maximum ( $\Phi = \pi/2$ ), or an intensity minimum ( $\Phi = \pi$ ). In addition, we will evaluate the detection efficiency  $\eta_\mu^d$  [Eq. (24)] and the phonon mean number occupation  $\bar{n}_\mu$  [Eq. (25)] for backward and forward detection and ideal feedback. These quantities will reveal in which situations ground-state cooling of 1D, 2D, and even 3D center-of-mass motion is possible.

We remind the reader [see Eq. (2)] that in this article we assume that 3D harmonic trapping with an equilibrium position at the focus with trap frequencies given by  $\Omega_\mu$  is possible when taking into account the optical forces generated by the laser beams. We do not specify, however, how this is implemented, i.e., whether using all-optical and gravitational forces [29–33], hybrid schemes combining low-frequency electric and optical forces [43–45], etc. In this way our analysis is

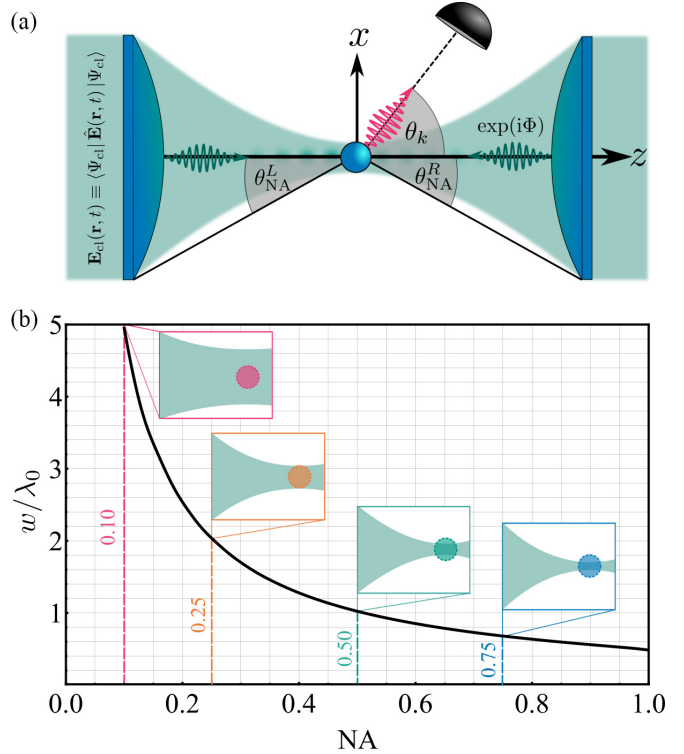


FIG. 2. (a) Sketch of the optical configuration. We consider one or two incoming  $x$ -polarized monochromatic Gaussian beams of frequency  $\omega_0$  propagating along the positive and negative  $z$  axes. The beams are focused by an anamorphic lens, which is assumed to be overfilled in order to achieve strong focusing at the focal point, where a dielectric sphere of radius  $R$  is placed. In the two-beam setup  $\Phi$  denotes the relative phase between the two counterpropagating beams. The IRPs  $\mathcal{I}_\mu(\theta_k, \phi_k)$  are defined with respect to the same coordinate system, where  $\theta_k$  denotes the angle between the positive- $z$  axis and the detector. (b) Waist  $w$  as a function of the numerical aperture NA of the lens. The insets show a sketch of the relative size of the sphere and the waist of the beam for  $R/\lambda_0 = 1$ .

very general; it even includes nonlevitating scenarios, e.g., a dielectric particle attached to a cantilever. We also remark that the IRPs and recoil heating rates calculated in this section are also relevant in situations where the particle is not harmonically trapped (e.g., in an inverted harmonic potential [46,52,54,55]). This is the case provided the sphere's center-of-mass fluctuations are small enough to justify the coupling linear with the center-of-mass position used at the starting point of the theory [see Eq. (1)].

#### A. Coherent amplitudes

The first task in applying our theory is to derive an expression for the coherent amplitudes  $\alpha_\kappa$  associated with the optical configuration we are considering (see Fig. 2). This is done by first deriving an expression for the classical electric field and then inferring  $\alpha_\kappa$  through Eq. (12). For notational convenience, we will label the lens placed at negative  $z$  values as left ( $L$ ) and the lens placed at positive- $z$  values as right ( $R$ ). The lenses can be used to focus and/or collect the scattered light. We derive the classical electric field of an incoming monochromatic  $x$ -polarized Gaussian beam

$\mathbf{E}_{\text{in}}(\mathbf{r}, t) = \text{Re}[\mathbf{E}_{\text{in}}(\mathbf{r}) \exp(-i\omega_0 t)]$  with mode profile  $\mathbf{E}_{\text{in}}(\mathbf{r})$  and frequency  $\omega_0$  focused by an aplanatic lens (see Fig. 2 and Appendix B for details). First, we focus on a single Gaussian beam propagating along the positive- $z$  axis (from the left) and whose focus coincides with the origin of coordinates (i.e., with the equilibrium position of the dielectric sphere). As shown in Appendix B, the corresponding coherent amplitudes  $\alpha_k^L$  for each polarization  $g = 1, 2$  read

$$\begin{aligned} \left[ \begin{array}{l} \alpha_1^L(k, \theta_k, \phi_k) \\ \alpha_2^L(k, \theta_k, \phi_k) \end{array} \right] &= \sqrt{\frac{4\pi k_0 P |\cos \theta_k|}{\hbar c^2 \sin^2 \theta_{\text{NA}}^L}} \frac{\delta(k - k_0)}{k_0^2} \\ &\times \exp\left(-\frac{\sin^2 \theta_k}{f_0^2 \sin^2 \theta_{\text{NA}}^L}\right) \left[ \begin{array}{l} i \sin \phi_k \\ \cos \phi_k \end{array} \right], \quad (27) \end{aligned}$$

where  $k_0 = 2\pi/\lambda_0 \equiv \omega_0/c$ . The parameters that determine the coherent amplitude are the optical power  $P$  of the focused field, the numerical aperture  $\text{NA} = \sin \theta_{\text{NA}}$  of the lens, and the filling factor  $f_0$ . We assume that the field overfills the lens,  $f_0 \gg 1$ , to guarantee maximum focusing of the beam [72]. A similar calculation enables us to compute the amplitudes for a beam propagating along the negative- $z$  axis (from the right), which can be written as  $\alpha_1^R(k, \theta_k, \phi_k) = \alpha_1^L(k, \theta_k, \phi_k)$  and  $\alpha_2^R(k, \theta_k, \phi_k) = -\alpha_2^L(k, \theta_k, \phi_k)$ . By combining the amplitudes of the left and right incoming beams and adding a relative phase  $\Phi$ , we obtain the coherent amplitude corresponding to two counterpropagating focused Gaussian beams in a standing-wave configuration, i.e.,  $\alpha_k^L + \alpha_k^R \exp(i\Phi)$ . Here the phase  $\Phi$  determines the intensity that scales as  $\cos^2(\Phi/2)$  at the particle position so that it lies at a node and antinode for  $\Phi = \pi$  and  $\Phi = 0$ , respectively. In Fig. 2(b) we show how the waist  $w$  of the focused Gaussian beam depends on the numerical aperture of the overfilled lens (see Appendix B 1 for details). As expected, the waist decreases rapidly with increasing numerical aperture and reaches a value on the order of the wavelength  $\lambda_0$ , which corresponds to the diffraction limit [72].

With the determined expression of the coherent amplitudes  $\alpha_k$  for the optical configuration of Fig. 2, we can now calculate the recoil heating rates  $\Gamma_\mu$  [Eq. (19)], the IRPs  $\mathcal{I}_\mu(\theta_k, \phi_k)$  [Eq. (22)], the detection efficiencies  $\eta_\mu^d$  [Eq. (24)] using the left or the right lens to collect the light, and the corresponding phonon mean-number occupation  $\bar{n}_\mu$  [Eq. (25)]. To do so, we will consider the physical parameters listed in Table I.

TABLE I. Parameters considered throughout this article.

Parameter	Description
$\epsilon = 2.07$	relative permittivity (silica) <sup>a</sup>
$\rho = 2200 \text{ kg/m}^3$	mass density (silica) <sup>b</sup>
$\lambda_0 = 1550 \text{ nm}$	laser wavelength
$P = 200 \text{ mW}$	power per laser beam
$f_0 = 10$	lens filling factor
$m_0 = 4.81 \times 10^{-26} \text{ kg}$	molecular mass (air)
$p = 10^{-9} \text{ mbar}$	gas pressure
$T = 300 \text{ K}$	gas temperature

<sup>a</sup>Reference [81].

<sup>b</sup>Reference [82].

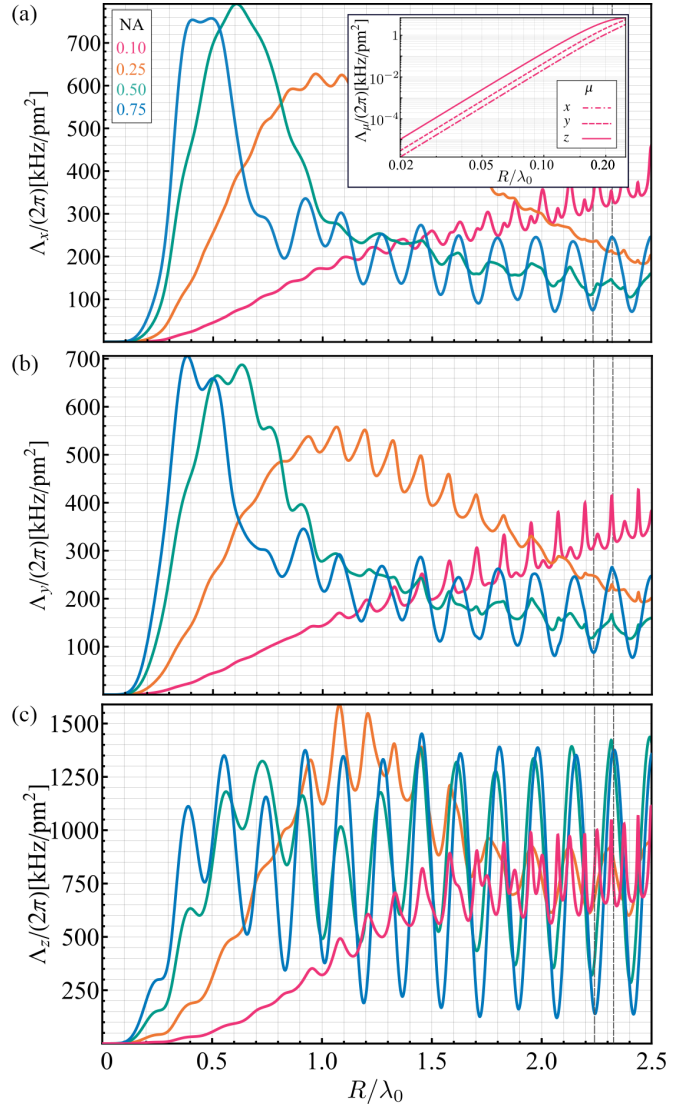


FIG. 3. Recoil localization parameter  $\Lambda_\mu = \Gamma_\mu/r_{0\mu}^2$  for a single focused  $x$ -polarized Gaussian beam propagating along the positive- $z$  axis as a function of the silica sphere's radius  $R/\lambda_0$  and the numerical aperture of the lens  $\text{NA} = 0.10, 0.25, 0.50$ , and  $0.75$ , for all three axes (a)  $\mu = x$ , (b)  $\mu = y$ , and (c)  $\mu = z$ . The values for the power, wavelength, and relative permittivity are listed in Table I. The inset in (a) shows a detailed view of the small-particle regime for all three axes at  $\text{NA} = 0.10$  on a log-log plot. The vertical gray dashed lines specify the radii for which the IRPs are shown in the last two columns in Fig. 4.

## B. Single focused beam

Let us first analyze the results for the running-wave configuration, where the left lens in Fig. 2 acts as a focusing and collection lens while the right lens acts as a collection lens only. In Fig. 3 we show  $\Lambda_\mu \equiv \Gamma_\mu/r_{0\mu}^2$ , which we hereafter call the recoil localization parameter.<sup>3</sup> The recoil

<sup>3</sup>In the context of position localization decoherence, the localization parameter is very relevant to describe the decoherence rate of quantum states that are spatially delocalized over scales larger than the zero-point motion [49,83,84].

localization parameter is the recoil heating rate divided by the squared zero-point motion and it hence does not depend on the trapping frequency  $\Omega_\mu$  [cf. Eq. (A44) in Appendix A 3]. Moreover, since  $\Gamma_\mu^g$  is also proportional to  $r_{0\mu}^2$  [see Eq. (26)], the phonon mean-number occupation  $\bar{n}_\mu$  [Eq. (25)] does also not depend on  $\Omega_\mu$ .

Figure 3 shows the recoil localization parameter for various numerical apertures NA and radii  $R$  ranging from the small-particle regime  $R/\lambda_0 \ll 1$  to the Lorenz-Mie regime  $R/\lambda_0 > 1$ . The inset in Fig. 3(a) shows the small-particle regime for all three axes and NA = 0.1 in greater detail. As expected, in the small-particle regime we recover the results obtained using the coupling rates in the point-dipole approximation (10), where the recoil localization parameter scales as  $\Lambda_\mu \propto (R/\lambda_0)^6$  [20,24]. Beyond the small-particle regime,  $\Lambda_\mu$  deviates from this polynomial scaling in size and transitions into an oscillatory behavior after reaching a maximum. The first maximum, which is not always global, is reached at smaller radii as one considers larger numerical apertures. The oscillatory features are most pronounced for  $\mu = z$  and NA = 0.75 and can be understood intuitively using the following simple model (cf. Appendix C). For large numerical apertures the waist of the focused beam is on the order of the wavelength [see Fig. 2(b)]. For spheres of radii  $R/\lambda_0 \gtrsim 1$  the system can therefore be modeled by a collimated beam that is normally incident on a dielectric slab of thickness  $2R$ , i.e., a Fabry-Pérot interferometer. Note that this regime is very different from the small-particle regime or from the case of small numerical apertures, where a nonvanishing intensity is incident across the whole surface of the sphere. Using this one-dimensional toy model, involving only two electromagnetic modes, we can show that the recoil localization parameter can be expressed in terms of the reflectance and transmittance of the interferometer (see Appendix C). These quantities oscillate with a period  $(4\sqrt{\epsilon})^{-1}$  in  $R/\lambda_0$ , which agrees with the oscillations observed in Fig. 3. Note that the typical values for zero-point motion of particles beyond the small-particle limit are in the picometer scale, and hence Fig. 3 shows that recoil heating rates  $\Gamma_\mu$  of several hundred kilohertz are expected. These recoil heating rates will be typically comparable to and larger than typical mechanical frequencies and hence feedback cooling schemes should be optimized to operate in these regimes.

In Fig. 4 we show the IRP for all three axes, a left lens with numerical aperture  $NA_L = 0.75$  in Fig. 4(a) and  $NA_L = 0.10$  in Fig. 4(b), a right lens with numerical aperture  $NA_R = 0.75$  in both Figs. 4(a) and 4(b), and a wide range of particle radii. Each panel contains the detection efficiency  $\eta_\mu^d$  [Eq. (24)] for the left lens (lower left corner) and right lens (lower right corner). All values for which the necessary condition for ground-state cooling, i.e.,  $\eta_\mu^d > \frac{1}{9}$ , is met are highlighted in blue (dark gray). The first column corresponds to the known IRPs [19] in the small-particle regime where almost all photons carrying information about the center-of-mass displacement along  $z$  are backscattered, leading to a large detection efficiency  $\mu_z^d = 0.55 \gg \frac{1}{9}$  for the high-NA configuration. The knowledge of the IRP in the small-particle regime has recently enabled the achievement of ground-state cooling along the  $z$  axis via active feedback [12,13]. While for  $R/\lambda_0 \leq 0.5$  the IRPs in the low- and high-NA configurations are very similar, we observe that, for larger radii,

their shape strongly depends on the numerical aperture  $NA_L$  of the focusing lens (left lens). For  $NA_L = 0.1$  the IRPs become increasingly sharply peaked in the forward direction as the radius increases. In contrast to the small-particle regime, the detection efficiency in the forward direction is orders of magnitude larger than the backward direction and exceeds the ground-state threshold of  $\frac{1}{9}$ . For  $NA_L = 0.75$  the angular distribution of the IRPs show more complex features. Note that for  $R/\lambda_0 = 2.24$  and 2.33 we observe a local minimum and maximum for  $\Lambda_\mu$  and NA = 0.75 along all three axes (recall the gray dashed lines in Fig. 3). In the corresponding IRPs in Fig. 4(a) we can see how a large recoil localization parameter goes hand in hand with a large number of backscattered photons, i.e., large reflectance in the Fabry-Pérot interferometer. For the  $z$  axis this leads to very high detection efficiencies of up to  $\eta_z^d = 0.8$ . As we show below, this trend is general since we obtain detection efficiencies that exceed the ground-state threshold for most radii in all other axes and for both forward and backward detection.

In Fig. 5 we show the detection efficiencies  $\eta_\mu^d$  at the left lens (dashed lines) and right lens (solid lines) as a function of the radius for all three axes. The threshold  $\eta_\mu^d = \frac{1}{9}$  is indicated with a horizontal dashed gray line. These detection efficiencies are then combined with the efficiency  $\eta_\mu^e$  associated with environmental information loss due to gas scattering [Eq. (24)] to obtain the minimum achievable mean phonon occupation number  $\bar{n}_\mu$  for ideal feedback [Eq. (25)] for the physical parameters given in Table I. The blue-shaded area highlights the regions for which  $\bar{n}_\mu < 1$ . Figure 5(a) shows how a high detection efficiency  $\eta_z^d$  in the backward direction (blue, dashed, highest curve at  $R/\lambda_0 \rightarrow 0$ ) enables the experimental realization of center-of-mass ground-state cooling using shot-noise-limited optical detection and active feedback [12,13]. While for  $\mu = x, y$  the detection efficiency in the small-particle limit is much smaller, all three axes reach comparably large values in the forward direction (solid) at  $R/\lambda_0 \simeq 0.5$ . The same can be said for the backward direction (dashed) for  $R/\lambda_0 > 1.0$ , where one again encounters the periodic features of the recoil localization parameter. Remarkably, this shows that there exists a broad range of parameters where simultaneous three-dimensional ground-state cooling is possible for the high-NA configuration. Similar conclusions can be drawn for the low-NA setup ( $NA_L = 0.10$  and  $NA_R = 0.75$ ) in Fig. 5. We observe how the detection efficiency in the forward direction (solid) quickly grows with increasing radius. In fact, the values oscillate around a value so large that three-dimensional ground-state cooling is also within reach for all three axes and  $R/\lambda_0 > 0.5$ .

### C. Standing wave

Let us now analyze the results for two focused  $x$ -polarized Gaussian beams counterpropagating along the  $z$  axis, where the lenses in Fig. 2 act as both focusing and collection lenses. Here we focus on the high-NA case, namely,  $NA_L = NA_R = 0.75$ . The results for  $NA_L = NA_R = 0.10$  are shown in Appendix D.

In Fig. 6 we show the recoil localization parameter for three values of the relative phase  $\Phi = 0, \pi/2, \pi$  (particle at the intensity maximum, intensity gradient maximum, and intensity minimum, respectively) as a function of  $R/\lambda_0$

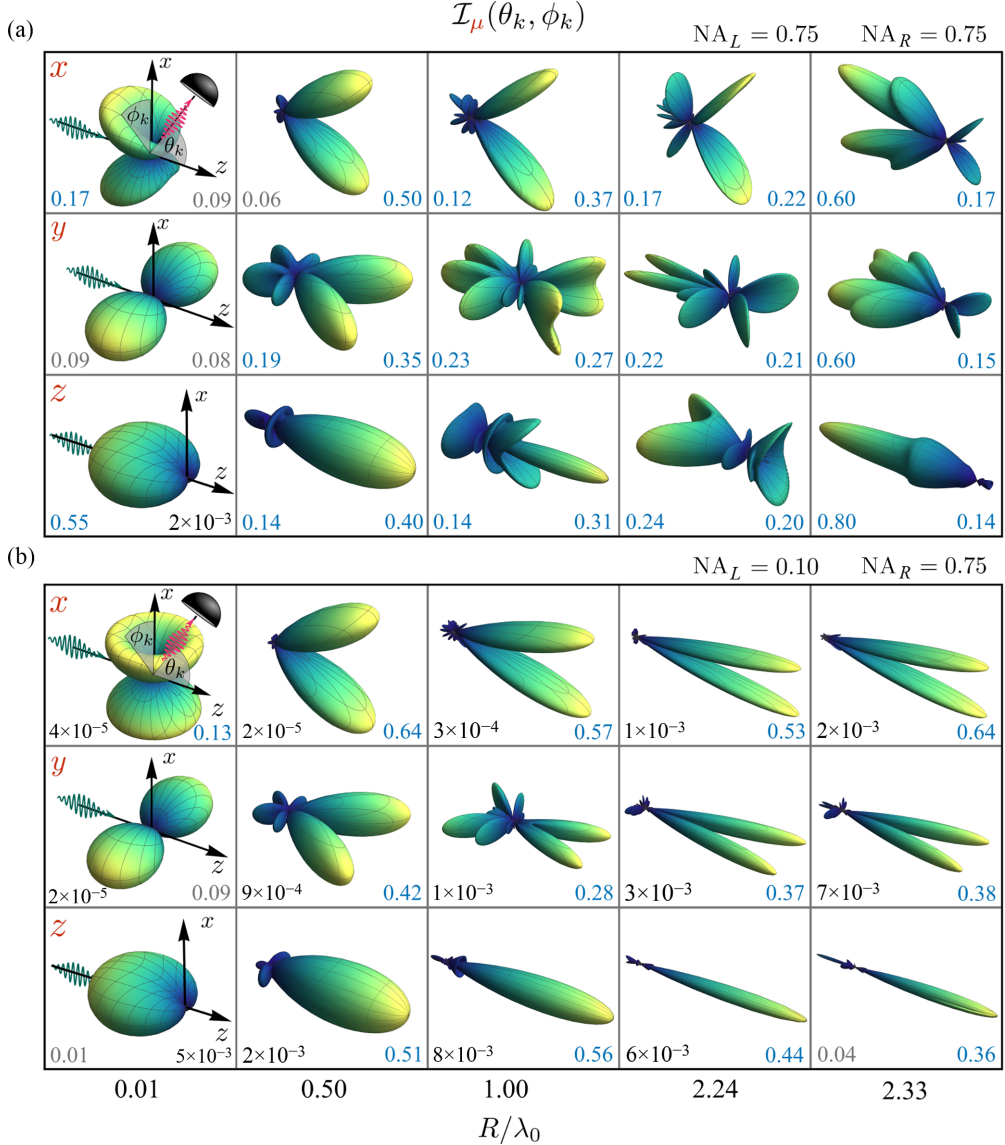


FIG. 4. Information radiation patterns  $\mathcal{I}_\mu(\theta_k, \phi_k)$  of a silica sphere and a single focused  $x$ -polarized Gaussian beam propagating along the positive- $z$  axis (reference frame in the first row). The value of the IRP is encoded in both the radial distance from the center and the color scale. The focusing lens has a numerical aperture (a)  $NA_L = 0.75$  and (b)  $NA_L = 0.10$ , while the collection lens has a numerical aperture  $NA_R = 0.75$  in both (a) and (b). The detection efficiency for the focusing lens and collection lens is shown in each panel (highlighted in blue for  $\eta_\mu^d > \frac{1}{9}$ ). Across the panels the value of  $R/\lambda_0$  is, for each column, constant and indicated below the last row.

ranging from the small-particle regime to the Lorenz-Mie regime for all three axes. Each panel contains an inset that shows the small-particle regime on a log-log plot in greater detail. Figure 6 shares many features with Fig. 3. The recoil localization parameters reach a maximum before they transition into an oscillatory behavior that is most pronounced for  $\mu = z$ , where the lines for the different relative phases overlap (see Appendix C for an explanation in terms of the model based on the Fabry-Pérot interferometer). Let us remark that within the point-dipole approximation and low-NA regime (e.g., two counterpropagating plane waves), the recoil heating rates have some features that have been discussed in the literature: (i) The sum  $\sum_\mu \Lambda_\mu$  is independent of  $\Phi$  (namely, the position of the particle in the standing wave) [85] and (ii)  $\Lambda_x = \Lambda_y = 0$

at  $\Phi = \pi$  (intensity maximum) [52]. Our theoretical treatment goes beyond the point-dipole approximation and low-NA assumptions and hence shows features beyond (i) and (ii). For instance, for low-NA (see Fig. 9 in Appendix D) we observe the expected  $\Lambda_z \propto (R/\lambda_0)^6$  scaling that can be derived using the coupling rates in the point-dipole approximation. However, for  $\mu = x, y$  and  $\Phi = \pi$  we observe a polynomial scaling of higher order, namely,  $\Lambda_{x,y} \propto (R/\lambda_0)^{10}$ . This is consistent with the fact that the coupling rates in the point-dipole approximation vanish when evaluated at this point and as a consequence the lowest-order term is the next nonvanishing term in the small-particle expansion.

In Fig. 7 we show the IRPs. For  $\Phi = 0, \pi$  the IRPs are bound to be symmetric due to the symmetry of the

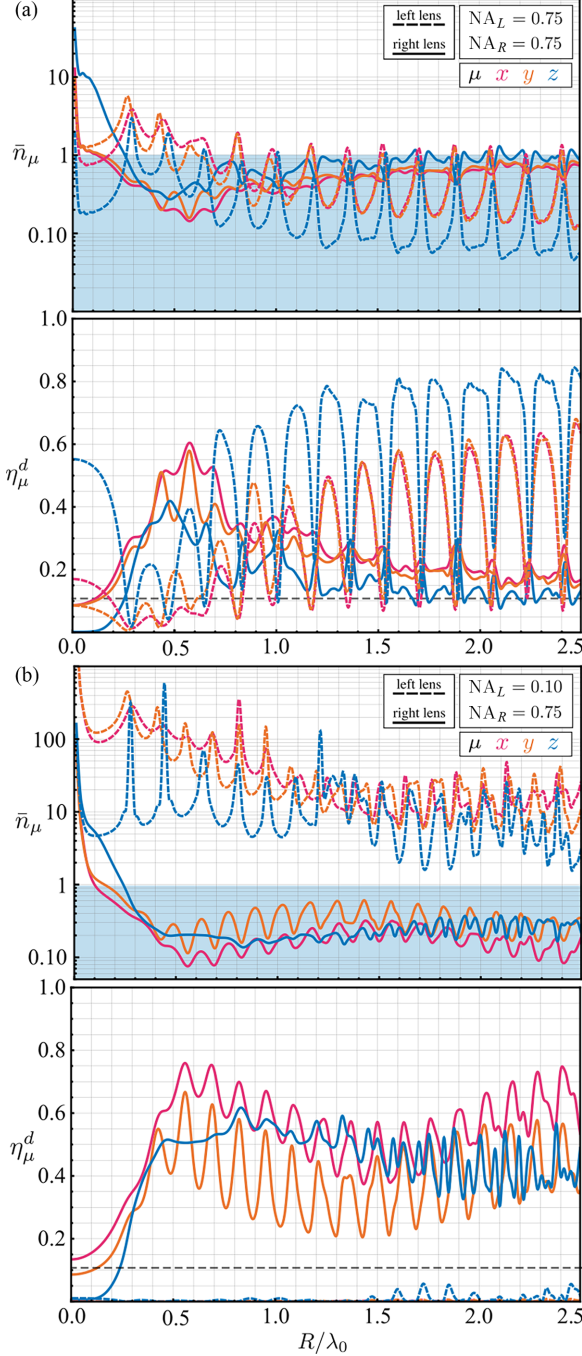


FIG. 5. Detection efficiencies  $\eta_\mu^d$  and minimum achievable mean phonon occupation number  $\bar{n}_\mu$  along  $x$ ,  $y$ , and  $z$  for ideal feedback as a function of  $R/\lambda_0$  for  $p = 10^{-9}$  mbar and  $T = 300$  K, at the same optical configuration as in Fig. 3. The dashed (solid) lines correspond to the values at the left (right) lens. The blue shaded area highlights the region where  $\bar{n}_\mu < 1$  and the gray dashed line shows  $\eta_\mu^d = \frac{1}{9}$ .

problem. This is not the case for  $\Phi = \pi/2$ , where the IRPs can show large asymmetries as shown by the detection efficiency values in the lower left and right corners. Similar to the running-wave configuration for  $NA_L = 0.75$  in Fig. 4(a), the IRPs show a complex angular distribution and the ground-state threshold detection efficiency  $\eta_\mu^d > \frac{1}{9}$  is reached for almost all axes, relative phases, and radii under consider-

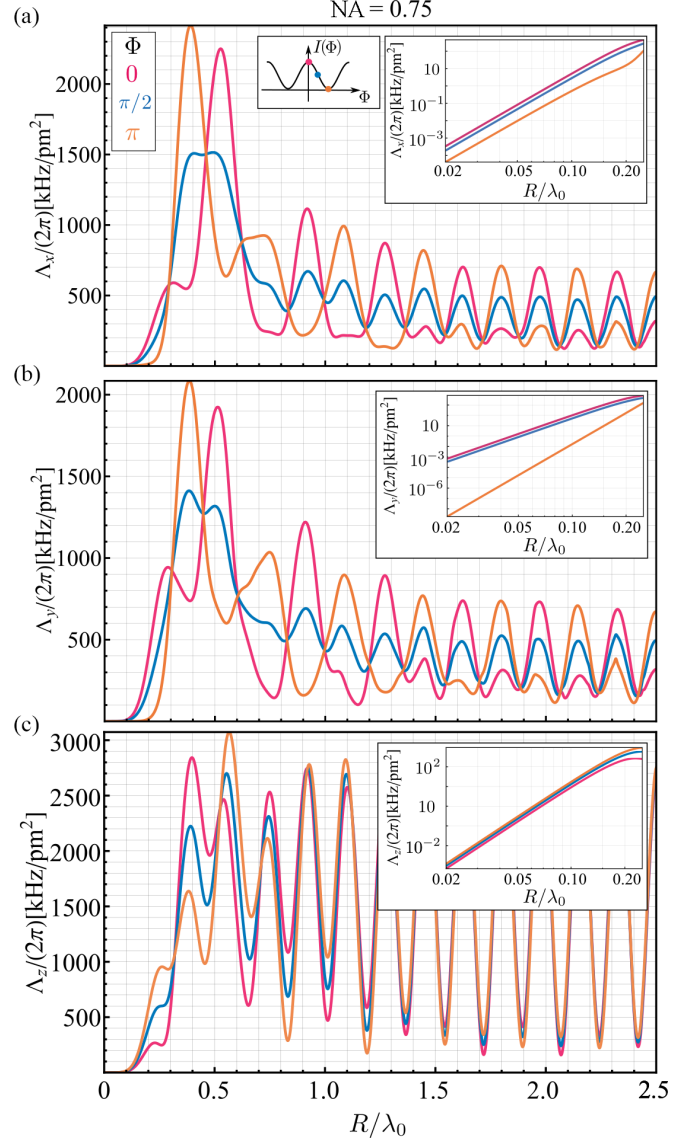


FIG. 6. Recoil localization parameter  $\Lambda_\mu = \Gamma_\mu / r_{0\mu}^2$  for two focused  $x$ -polarized Gaussian beams counterpropagating along the  $z$  axis as a function of the silica sphere's radius  $R/\lambda_0$  for all three axes (a)  $\mu = x$ , (b)  $\mu = y$ , and (c)  $\mu = z$ . The values for the power, wavelength, and relative permittivity are listed in Table I. Each panel shows the recoil localization parameter for  $\Phi = 0$ ,  $\pi/2$ ,  $\pi$ , and  $NA = 0.75$  and an inset with a detailed view of the small-particle regime for all three relative phases on a log-log plot. The inset in (a) maps the relative phase  $\Phi$  to the corresponding intensity at the origin.

ation. This is explicitly shown in Fig. 8, where we show the detection efficiencies at the left (dashed lines) and right (solid lines) lenses as a function of the radius for all axes and relative phases [ $\Phi = 0$ ,  $\pi/2$ , and  $\pi$  in Figs. 8(a)–8(c), respectively]. The detection efficiencies are then combined with the efficiency  $\eta_\mu^e$  associated with environmental information loss due to gas scattering [Eq. (24)] to obtain the minimum achievable mean phonon occupation number  $\bar{n}_\mu$  for ideal feedback [Eq. (25)] and the gas pressure and temperature in Table I. While in the small-particle regime the detection

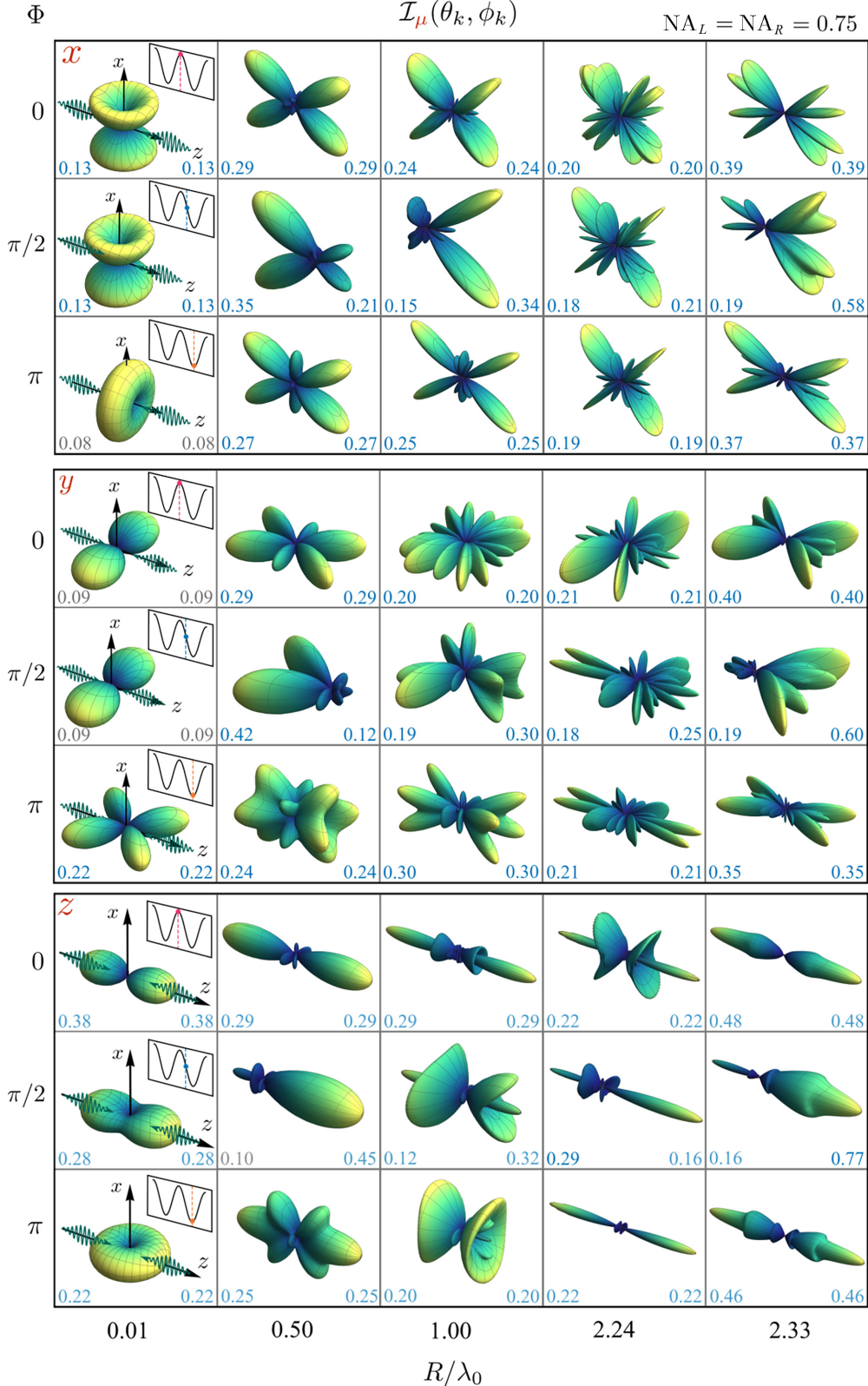


FIG. 7. Information radiation patterns  $\mathcal{I}_z(\theta_k, \phi_k)$  of a silica sphere, two focused  $x$ -polarized Gaussian beams counterpropagating parallel to the  $z$  axis (reference frame in the first row), and relative phases  $\Phi = 0, \pi/2, \pi$  (the corresponding intensity at the origin is shown as an inset in the first column). The value of the IRP is encoded in both the radial distance from the center and the color scale. The two focusing lenses have a numerical aperture  $NA_L = NA_R = 0.75$ . The detection efficiencies for the left and right lenses are shown in each panel (highlighted in blue for  $\eta_\mu^d > \frac{1}{9}$ ). Across the panels the value of  $R/\lambda_0$  is, for each column, constant and indicated below the last row.

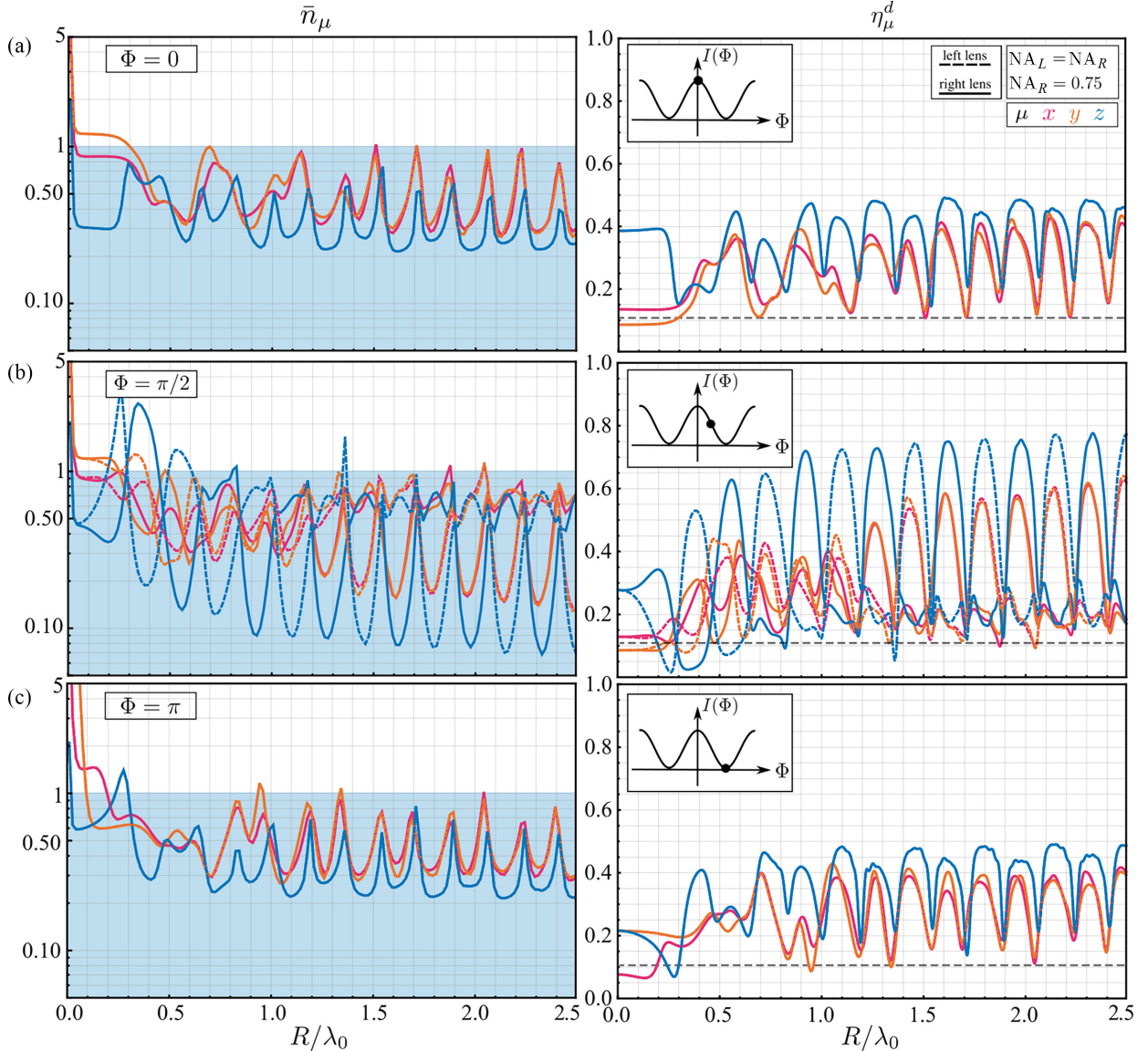


FIG. 8. Detection efficiencies  $\eta_\mu^d$  and minimum achievable mean phonon occupation number  $\bar{n}_\mu$  along  $x$ ,  $y$ , and  $z$  for ideal feedback as a function of  $R/\lambda_0$  for  $p = 10^{-9}$  mbar and  $T = 300$  K, at the same optical configuration as in Fig. 7, and for (a)  $\Phi = 0$ , (b)  $\Phi = \pi/2$ , and (c)  $\Phi = \pi$  with an inset that maps the relative phase  $\Phi$  to the corresponding intensity at the origin. The dashed (solid) lines correspond to the values at the left (right) lens. The blue shaded area highlights the region where  $\bar{n}_\mu < 1$  and the gray dashed line shows  $\eta_\mu^d = \frac{1}{9}$ .

efficiency along  $x$  and  $y$  lies below threshold for  $\Phi = \pi$  and  $\Phi = 0, \pi/2$  respectively, we see that for almost all the remaining parameters 3D ground-state cooling is possible for a broad range of parameters. Interestingly, at  $\Phi = \pi/2$  and for the motion along the standing-wave axis ( $z$  axis), we observe marked oscillations as a function of  $R/\lambda_0$  between very high collection efficiency and hence low  $\bar{n}_z$  alternating between the left and right lens, something that one can understand using the Fabry-Pérot interferometer toy model (Appendix C). Finally, let us emphasize that the IRPs and recoil heating rates (also called backaction noise rates) obtained at  $\Phi = \pi$  (intensity minimum) are particularly relevant in scenarios where the inverted harmonic optical potential is used for exponentially expanding the center-of-mass position probability distribution, which is of interest for enhancing optical position detection [52,54,55].

## V. CONCLUSION

In the first part of this article we developed a quantum theory of light interacting with the center-of-mass degrees of freedom of a dielectric sphere of arbitrary refractive index and size. The theory assumes the fluctuations of the center of mass to be small enough so that the light-matter coupling is linear in the center-of-mass position. This theory makes use of the quantization of the electromagnetic field in the presence of a dielectric sphere of arbitrary refractive index and size, a task thoroughly derived in [58] based on [59]. This point is key, as the use of normalized scattering eigenmodes, as opposed to plane-wave modes, clearly reveals the Stokes and anti-Stokes processes which are responsible for describing the optomechanical physics of the problem. Furthermore, the spherical shape of the dielectric object allows us to perform an

analytical treatment using many of the available analytical tools in spherical coordinates, thereby leading to optomechanical coupling rates, recoil heating rates, and information radiation patterns, which can be efficiently evaluated. We emphasize, however, that we expect the theoretical methods of this article to be extendable to other shapes and other degrees of freedom (e.g., rotations [60–70] and internal acoustic phonons [86–89]). We expect the recipe to be the same: (i) Quantize the electromagnetic field with the object at equilibrium (cf. [58]). (ii) Obtain the equations of motion of the relevant degrees of freedom driven by an electromagnetic force or torque [cf. Eq. (4)], which can be derived from a Hamiltonian with a linear coupling to the relevant degrees of freedom [cf. Eq. (1)]. (iii) Using classical electrodynamics express the electromagnetic force or torque acting on the degrees of freedom of interest written in terms of the electromagnetic fields [cf. Eq. (5)]. (iv) Introduce the quantized electromagnetic fields in the presence of the object at equilibrium [cf. Eqs. (6) and (7)] into the initial Hamiltonian to obtain a Hamiltonian describing the interaction between bosonic modes [cf. Eq. (8)] and the corresponding optomechanical couplings [cf. Eq. (9)]. (v) Linearize the theory using a classical electromagnetic field of relevance [cf. Eq. (12)] to obtain a quadratic Hamiltonian [cf. Eq. (13)] that can be used to evaluate recoil heating rates and information radiation patterns.

In the second part of this article we showed how the developed theory can be used to evaluate the recoil heating rates and the information radiation patterns for a focused beam in either a running-wave or a standing-wave configuration. These results are relevant since in situations where the recoil heating rate dominates any other source of noise, the information radiation pattern is key to enabling center-of-mass ground-state cooling via active feedback. We have shown that in this experimentally feasible configuration, high collection efficiency of the light carrying information about the center-of-mass degrees of freedom can be achieved for particles comparable to and larger than the optical wavelength. This is possible not only in one degree of freedom as it happens for small particles, but for the three degrees of freedom, thereby allowing for simultaneously three-dimensional center-of-mass ground-state cooling.

Our work opens many research directions for further exploration. (i) As mentioned above, one could extend the results of this article to other shapes and degrees of freedom, such as rotation and internal acoustic vibrations. (ii) Large particles support whispering gallery modes, which can potentially enhance the coupling strength. These modes possess a high angular momentum and can be excited by off-axis focused Gaussian beams (see [90]). (iii) While we have focused on silica particles, other dielectric particles have a much higher refractive index (e.g., silicon) which enhances optical resonances that could be exploited for optomechanics [91]. It would be particularly interesting to study and exploit the optical interaction between several dielectric particles beyond the point-dipole regime [7,92–95] and in the quantum regime. (iv) The fact that dielectric particles beyond the point-dipole regime experience large recoil heating rates, comparable to and even larger than the mechanical frequencies, hints at the possibility to enter the strong quantum optomechanical regime [9,96,97] in free space, which could have applications

in generating quantum interfaces between light and center-of-mass motion without the use of optical resonators. (v) Our quantum theory allows us to consider the injection of vacuum squeezing to modify the trade-off between imprecision and backaction noise and obtain displacement sensitivities beyond the standard quantum limit, as recently discussed in [98] in the point-dipole approximation. This could be particularly interesting in the context of using micrometer-size dielectric spheres for the search of new physics, such as dark matter [31,32,34–42].

## ACKNOWLEDGMENTS

We acknowledge useful discussions with M. Aspelmeyer, M. Frimmer, D. Hümmer, A. Militaru, L. Novotny, and M. Rossi. This research was supported by the European Union’s Horizon 2020 research and innovation program under Grant Agreement No. 863132 (IQLev) and by the European Research Council under Grant Agreement No. 951234 (Q-Xtreme ERC-2020-SyG).

## APPENDIX A: DERIVATION OF EXPLICIT EXPRESSIONS

In this Appendix we derive the explicit expressions for the central quantities in the main text. First we derive in Appendix A 1 an explicit expression for the coupling rates. Then we derive in Appendix A 2 an explicit expression for the Stokes and anti-Stokes transition amplitudes in the asymptotic limit. Finally, we combine these results in Appendix A 3 by deriving explicit expressions for the information radiation patterns and recoil heating rates.

### 1. Derivation of the coupling rates

In this section we show how to derive an analytical expression for the coupling rates  $g_{\kappa\kappa'\mu}$  starting from Eq. (9), that is,

$$g_{\kappa\kappa'\mu} = r_{0\mu} \frac{\sqrt{\omega_\kappa \omega_{\kappa'}}}{2} \lim_{r \rightarrow \infty} r^2 \int d\Omega (\mathbf{e}_r \cdot \mathbf{e}_\mu) \\ \times \left( \mathbf{F}_\kappa^*(\mathbf{r}) \cdot \mathbf{F}_{\kappa'}(\mathbf{r}) + \frac{1}{kk'} \nabla \times \mathbf{F}_\kappa^*(\mathbf{r}) \cdot \nabla \times \mathbf{F}_{\kappa'}(\mathbf{r}) \right). \quad (A1)$$

In particular, we show that the coupling rates for a dielectric sphere of arbitrary refractive index and size can be expressed as a sum over discrete angular momentum indices  $l = 1, 2, \dots$  and  $m = -l, -l+1, \dots, l$  and polarization indices  $p \in \{\text{TE}, \text{TM}\}$ .

We proceed in three steps (see details below). First, we insert in Eq. (A1) the explicit far-field expression of the normalized scattering eigenmodes that can be written in terms of the vector spherical harmonic  $\mathbf{X}_l^m(\theta, \phi)$ . This leads to an integrand that consists of a sum of products of two vector spherical harmonics of different order  $l$  and a  $\mu$ -dependent term, that is,  $\mathbf{e}_r \cdot \mathbf{e}_\mu$ . As a second step we derive an analytical expression for these angular integrals. Finally, we use trigonometric identities to further simplify the analytical expression for the coupling rates  $g_{\kappa\kappa'\mu}$ .

Let us start now by deriving the explicit far-field expression of the scattering eigenmodes  $\mathbf{F}_\kappa(\mathbf{r})$  in terms of vector spherical harmonics. In [58] we derived an expression for the scattering eigenmodes in terms of the spherical eigenmodes in spherical coordinates, namely,  $\mathbf{F}_\kappa(\mathbf{r}) = k^{-1} \sum_{lmp} \bar{c}_{lmg}^p(\theta_k, \phi_k) \mathbf{S}_{lmg}^p(k; \mathbf{r})$ . The spherical eigenmodes  $\mathbf{S}_{lmg}^p(k; \mathbf{r})$  are characterized by the discrete angular momentum indices  $l$  and  $m$  and polarization indices  $p$  and can be mapped to the electromagnetic fields of electric and magnetic multipoles. The coefficients  $\bar{c}_{lmg}^p$  can be shown to read

$$\begin{aligned} \bar{c}_{lmg}^{\text{TE}}(\theta_k, \phi_k) &\equiv \Theta(l - |m|) c_{lmg}^{\text{TE}}(\theta_k, \phi_k) \\ &= i^l \Theta(l - |m|) \mathbf{X}_l^{m*}(\theta_k, \phi_k) \cdot \mathbf{e}_g(\theta, \phi), \end{aligned} \quad (\text{A2})$$

$$\begin{aligned} \bar{c}_{lmg}^{\text{TM}}(\theta_k, \phi_k) &\equiv \Theta(l - |m|) c_{lmg}^{\text{TM}}(\theta_k, \phi_k) \\ &= i^l \Theta(l - |m|) \mathbf{X}_l^{m*}(\theta_k, \phi_k) \cdot [\mathbf{e}_r \times \mathbf{e}_g(\theta, \phi)], \end{aligned} \quad (\text{A3})$$

where  $\mathbf{X}_l^m(\theta, \phi)$  denotes a vector spherical harmonic as defined in [58, 99],  $\Theta(x)$  denotes the Heaviside Theta function with  $\Theta(0) = 1$ , and the two transverse polarization vectors read  $\mathbf{e}_1(\theta, \phi) \equiv i\mathbf{e}_\phi(\theta, \phi)$  and  $\mathbf{e}_2(\theta, \phi) \equiv \mathbf{e}_\theta(\theta, \phi)$ . For notational convenience the sum runs over all  $l$  and  $m$ , where the restriction to  $m = -l, -l+1, \dots, l$  is taken care of by the expansion coefficients  $\bar{c}_{lmg}^p(\theta_k, \phi_k)$  that vanish for  $l < |m|$ .

The spherical eigenmodes  $\mathbf{S}_{lmg}^p(k; \mathbf{r})$  are separable in the radial and angular variables  $r$ ,  $\theta$ , and  $\phi$ . As shown explicitly in [58], their dependence on the radial coordinate is given by the spherical Bessel and Hankel functions  $j_l(x)$  and  $h_l(x)$  of the first kind and order  $l$ . Their dependence on

the angular coordinates is given by vector spherical harmonics. Using  $\lim_{r \rightarrow \infty} j_l(kr) = (kr)^{-1} \sin(kr - l\pi/2)$  and  $\lim_{r \rightarrow \infty} h_l(kr) = -i(kr)^{-1} \exp[i(kr - l\pi/2)]$ , it follows that

$$\begin{aligned} \lim_{r \rightarrow \infty} \mathbf{F}_\kappa(\mathbf{r}) &= \frac{1}{kr} \sum_{lm} [X_{lmg}^{\text{TE}}(kr, \theta_k, \phi_k) \mathbf{X}_l^m(\theta, \phi) \\ &\quad + Y_{lmg}^{\text{TM}}(kr, \theta_k, \phi_k) \mathbf{Y}_l^m(\theta, \phi)], \end{aligned} \quad (\text{A4})$$

$$\begin{aligned} \lim_{r \rightarrow \infty} \nabla \times \mathbf{F}_\kappa(\mathbf{r}) &= \frac{ik}{kr} \sum_{lm} [X_{lmg}^{\text{TM}}(kr, \theta_k, \phi_k) \mathbf{X}_l^m(\theta, \phi) \\ &\quad - Y_{lmg}^{\text{TE}}(kr, \theta_k, \phi_k) \mathbf{Y}_l^m(\theta, \phi)]. \end{aligned} \quad (\text{A5})$$

The far-field expressions of the normalized scattering eigenmodes are written in terms of a linear combination of the vector spherical harmonics  $\mathbf{X}_l^m(\theta, \phi)$  and  $\mathbf{Y}_l^m(\theta, \phi) = -i\mathbf{e}_r \times \mathbf{X}_l^m(\theta, \phi)$ . The radial functions  $X_{lmg}^p(kr, \theta_k, \phi_k)$  and  $Y_{lmg}^p(kr, \theta_k, \phi_k) = X_{lmg}^p(kr - \pi/2, \theta_k, \phi_k)$  read

$$\begin{aligned} X_{lmg}^p(kr, \theta_k, \phi_k) &= \sqrt{\frac{2}{\pi}} \bar{c}_{lmg}^p(\theta_k, \phi_k) \{ \sin(kr - l\pi/2) \\ &\quad - (-i)^l \sin \varphi_l^p \exp[i(kr - \varphi_l^p)] \}. \end{aligned} \quad (\text{A6})$$

The explicit expression for  $\varphi_l^p$  in terms of the Lorenz-Mie coefficients depend on the sphere's radius  $R$  and relative permittivity  $\epsilon$  and can be found in [58]. They can also be expressed in terms of the Mie coefficients in [100], namely,  $a_l \equiv i \sin \varphi_l^{\text{TM}} \exp(-i\varphi_l^{\text{TM}})$  and  $b_l = i \sin \varphi_l^{\text{TE}} \exp(-i\varphi_l^{\text{TE}})$ . Inserting Eqs. (A4) and (A5) in Eq. (A1) and using  $\omega_k = ck$ , we arrive at

$$\begin{aligned} g_{\kappa\kappa'\mu} &= \frac{cr_0\mu}{2\sqrt{kk'}} \sum_{lm} \sum_{l'm'} \int d\Omega(\mathbf{e}_r \cdot \mathbf{e}_\mu) \{ [X_{lmg}^{\text{TE}}(kr, \theta_k, \phi_k) \mathbf{X}_l^m(\theta, \phi) + Y_{lmg}^{\text{TM}}(kr, \theta_k, \phi_k) \mathbf{Y}_l^m(\theta, \phi)]^* \\ &\quad \cdot [X_{l'm'g'}^{\text{TE}}(k'r, \theta_{k'}, \phi_{k'}) \mathbf{X}_{l'}^{m'}(\theta, \phi) + Y_{l'm'g'}^{\text{TM}}(k'r, \theta_{k'}, \phi_{k'}) \mathbf{Y}_{l'}^{m'}(\theta, \phi)] \\ &\quad + [X_{lmg}^{\text{TM}}(kr, \theta_k, \phi_k) \mathbf{X}_l^m(\theta, \phi) - Y_{lmg}^{\text{TE}}(kr, \theta_k, \phi_k) \mathbf{Y}_l^m(\theta, \phi)]^* \\ &\quad \cdot [X_{l'm'g'}^{\text{TM}}(k'r, \theta_{k'}, \phi_{k'}) \mathbf{X}_{l'}^{m'}(\theta, \phi) - Y_{l'm'g'}^{\text{TE}}(k'r, \theta_{k'}, \phi_{k'}) \mathbf{Y}_{l'}^{m'}(\theta, \phi)] \}. \end{aligned} \quad (\text{A7})$$

In order to further evaluate Eq. (A7) we need to find an expression for the angular integrals containing the product of two vector spherical harmonics and the  $\mu$ -dependent term  $\mathbf{e}_r \cdot \mathbf{e}_\mu$ , that is,

$$I_{XX}^\mu = I_{YY}^\mu \equiv \int_{\mathbb{S}^2} d\Omega(\mathbf{e}_r \cdot \mathbf{e}_\mu) \mathbf{X}_l^{m*}(\theta, \phi) \cdot \mathbf{X}_{l'}^{m'}(\theta, \phi), \quad (\text{A8})$$

$$I_{XY}^\mu \equiv \int_{\mathbb{S}^2} d\Omega(\mathbf{e}_r \cdot \mathbf{e}_\mu) \mathbf{X}_l^{m*}(\theta, \phi) \cdot \mathbf{Y}_{l'}^{m'}(\theta, \phi), \quad (\text{A9})$$

$$I_{YX}^\mu \equiv \int_{\mathbb{S}^2} d\Omega(\mathbf{e}_r \cdot \mathbf{e}_\mu) \mathbf{Y}_l^{m*}(\theta, \phi) \cdot \mathbf{X}_{l'}^{m'}(\theta, \phi), \quad (\text{A10})$$

where we have used that  $[\mathbf{Y}_l^m(\theta, \phi)]^* \cdot \mathbf{Y}_{l'}^{m'}(\theta, \phi) = [\mathbf{X}_l^m(\theta, \phi)]^* \cdot \mathbf{X}_{l'}^{m'}(\theta, \phi)$ . Using the results of [73], it is possible to derive an analytical expression for each of the above terms, namely,

$$\begin{aligned} I_{XX}^\mu &= \sqrt{\frac{l(l+2)(l-m'+1)(l-m')}{(2l+3)(2l+1)}} \frac{\delta_{l+1l'}\delta_{mm'+1}}{2l+2} - \sqrt{\frac{l'(l'+2)(l'+m'+2)(l'+m'+1)}{(2l'+3)(2l'+1)}} \frac{\delta_{ll'+1}\delta_{mm'+1}}{2l'+2} \\ &\quad + \sqrt{\frac{l'(l'+2)(l'-m+1)(l'-m)}{(2l'+3)(2l'+1)}} \frac{\delta_{ll'+1}\delta_{m+1m'}}{2l'+2} - \sqrt{\frac{l(l+2)(l+m+2)(l+m+1)}{(2l+3)(2l+1)}} \frac{\delta_{l+1l'}\delta_{m+1m'}}{2l+2}, \end{aligned} \quad (\text{A11})$$

$$I_{XY}^x = I_{YX}^x = -\frac{\sqrt{(l+m)(l-m+1)}}{2l(l+1)}\delta_{ll'}\delta_{mm'+1} - \frac{\sqrt{(l-m)(l+m+1)}}{2l(l+1)}\delta_{ll'}\delta_{m+1m'}, \quad (\text{A12})$$

$$\begin{aligned} I_{XX}^y &= \sqrt{\frac{l(l+2)(l-m'+1)(l-m')}{(2l+3)(2l+1)}}\frac{\delta_{l+1l'}\delta_{mm'+1}}{2il+2i} - \sqrt{\frac{l'(l'+2)(l'+m'+2)(l'+m'+1)}{(2l'+3)(2l'+1)}}\frac{\delta_{ll'+1}\delta_{mm'+1}}{2il'+2i} \\ &\quad - \sqrt{\frac{l'(l'+2)(l'-m+1)(l'-m)}{(2l'+3)(2l'+1)}}\frac{\delta_{ll'+1}\delta_{m+1m'}}{2il'+2i} + \sqrt{\frac{l(l+2)(l+m+2)(l+m+1)}{(2l+3)(2l+1)}}\frac{\delta_{l+1l'}\delta_{m+1m'}}{2il+2i}, \end{aligned} \quad (\text{A13})$$

$$I_{YX}^y = I_{XY}^y = -\frac{\sqrt{(l+m)(l-m+1)}}{2il(l+1)}\delta_{ll'}\delta_{mm'+1} + \frac{\sqrt{(l-m)(l+m+1)}}{2il(l+1)}\delta_{ll'}\delta_{m+1m'}, \quad (\text{A14})$$

$$I_{XX}^z = \sqrt{\frac{l(l+2)(l+m'+1)(l-m'+1)}{(2l+3)(2l+1)}}\frac{\delta_{l+1l'}\delta_{mm'}}{l+1} + \sqrt{\frac{l'(l'+2)(l'+m+1)(l'-m+1)}{(2l'+3)(2l'+1)}}\frac{\delta_{ll'+1}\delta_{mm'}}{l'+1}, \quad (\text{A15})$$

$$I_{XY}^z = -\frac{m}{l(l+1)}\delta_{ll'}\delta_{mm'} = I_{YX}^z. \quad (\text{A16})$$

Note that all integrals contain a Kronecker delta in  $l'$  and  $m'$ . Thus, inserting Eqs. (A11)–(A16) in Eq. (A7) leads to an expression for the coupling rates  $g_{\kappa\kappa'\mu}$  that is written as a *single* sum over the discrete angular momentum and polarization indices. For each  $\mu \in \{x, y, z\}$  the sum runs over terms that are all proportional to one of the two following combinations of products of the radial functions  $X_{lmg}^p(kr, \theta_k, \phi_k)$  and  $Y_{lmg}^p(kr, \theta_k, \phi_k)$ :

$$\begin{aligned} X_{lmg}^{p*}(kr, \theta_k, \phi_k)X_{l'm'g'}^p(k'r, \theta_{k'}, \phi_{k'}) &+ Y_{lmg}^{p*}(kr, \theta_k, \phi_k)Y_{l'm'g'}^p(k'r, \theta_{k'}, \phi_{k'}) \\ &= \frac{2}{\pi}\bar{c}_{lmg}^{p*}(\theta_k, \phi_k)\bar{c}_{l'm'g'}^p(\theta_{k'}, \phi_{k'})\exp[i(\varphi_l^p - \varphi_{l'}^p)]\cos[(l-l')\pi/2 + \varphi_l^p - \varphi_{l'}^p], \end{aligned} \quad (\text{A17})$$

$$\begin{aligned} X_{lmg}^{p*}(kr, \theta_k, \phi_k)Y_{l'm'g'}^{p'}(k'r, \theta_{k'}, \phi_{k'}) &- Y_{lmg}^{p*}(kr, \theta_k, \phi_k)X_{l'm'g'}^{p'}(k'r, \theta_{k'}, \phi_{k'}) \\ &= \frac{2}{\pi}\bar{c}_{lmg}^{p*}(\theta_k, \phi_k)\bar{c}_{l'm'g'}^{p'}(\theta_{k'}, \phi_{k'})\exp[i(\varphi_l^p - \varphi_{l'}^{p'})]\sin[(l-l')\pi/2 + \varphi_l^p - \varphi_{l'}^{p'}]. \end{aligned} \quad (\text{A18})$$

These equations immediately follow from standard trigonometric identities. As expected, this leads to an expression for the coupling rates that is independent of the radial variable  $r$ .

Note that Eqs. (A17) and (A18) do in principle depend on  $k$  and  $k'$  independently through  $\varphi_l^p$  and  $\varphi_{l'}^{p'}$ . Here we derive coupling rates for processes where photons at frequency  $\omega_0$  interact with center-of-mass phonons with frequencies  $\Omega_\mu$  that are many orders of magnitude smaller  $\Omega_\mu \ll \omega_0$ . In light of this and in order to simplify the notation, we therefore approximate  $k \simeq k'$ . Combining all these results, it immediately follows that the coupling rates can be compactly written as

$$g_{\kappa\kappa'\mu} = \frac{icr_0\mu}{2\pi\sqrt{kk'}} \sum_{lmp} \bar{c}_{lmg}^{p*}(\theta_k, \phi_k)a_{lmg}^{\mu p}(\theta_{k'}, \phi_{k'}). \quad (\text{A19})$$

Here we have used the fact that the sum runs over all  $l \in \mathbb{N}^+$  and  $m \in \mathbb{Z}$ , which allows for a simple shifting of the summation indices. The above representation is particularly advantageous for deriving an expression for the IRPs and the recoil heating rates in Appendix A 3. The explicit form of  $a_{lmg}^{\mu p}(\theta_k, \phi_k)$  reads

$$\begin{aligned} a_{lmg}^{xp}(\theta_k, \phi_k) &= \sqrt{\frac{l(l+2)(l-m+2)(l-m+1)}{(2l+3)(2l+1)(2l+2)^2}}\bar{c}_{l+1m-1g}^p S_l^p - \sqrt{\frac{(l-1)(l+1)(l-m)(l-m-1)}{(2l+1)(2l-1)(2l)^2}}\bar{c}_{l-1m+1}^p (S_{l-1}^p)^* \\ &\quad - \sqrt{\frac{l(l+2)(l+m+2)(l+m+1)}{(2l+3)(2l+1)(2l+2)^2}}\bar{c}_{l+1m+1g}^p S_l^p + \sqrt{\frac{(l-1)(l+1)(l+m)(l+m-1)}{(2l+1)(2l-1)(2l)^2}}\bar{c}_{l-1m-1g}^p (S_{l-1}^p)^* \\ &\quad - \frac{\sqrt{(l+m)(l-m+1)}}{2l(l+1)}\bar{c}_{lm-1g}^{\bar{p}} R_l^{\bar{p}} - \frac{\sqrt{(l+m+1)(l-m)}}{2l(l+1)}\bar{c}_{lm+1g}^{\bar{p}} R_l^{\bar{p}}, \end{aligned} \quad (\text{A20})$$

$$ia_{lmg}^{yp}(\theta_k, \phi_k) = \sqrt{\frac{l(l+2)(l-m+2)(l-m+1)}{(2l+3)(2l+1)(2l+2)^2}}\bar{c}_{l+1m-1g}^p S_l^p + \sqrt{\frac{(l-1)(l+1)(l-m)(l-m-1)}{(2l+1)(2l-1)(2l)^2}}\bar{c}_{l-1m+1}^p (S_{l-1}^p)^*$$

$$+ \sqrt{\frac{l(l+2)(l+m+2)(l+m+1)}{(2l+3)(2l+1)(2l+2)^2}} \bar{c}_{l+1m+1g}^p S_l^p + \sqrt{\frac{(l-1)(l+1)(l+m)(l+m-1)}{(2l+1)(2l-1)(2l)^2}} \bar{c}_{l-1m-1g}^p (S_{l-1}^p)^* \\ - \frac{\sqrt{(l+m)(l-m+1)}}{2l(l+1)} \bar{c}_{lm-1g}^p R_l^p + \frac{\sqrt{(l+m+1)(l-m)}}{2l(l+1)} \bar{c}_{lm+1g}^p R_l^p, \quad (\text{A21})$$

$$\tilde{a}_{lmg}^p(\theta_k, \phi_k) = \sqrt{\frac{l(l+2)[(l+1)^2 - m^2]}{(2l+3)(2l+1)(l+1)^2}} \bar{c}_{l+1mg}^p S_l^p - \sqrt{\frac{(l^2-1)(l^2-m^2)}{(4l^2-1)l^2}} \bar{c}_{l-1mg}^p (S_{l-1}^p)^* - \frac{m}{l(l+1)} \bar{c}_{lmg}^p R_l^p, \quad (\text{A22})$$

where we have defined  $\overline{\text{TE}} \equiv \text{TM}$ ,  $\overline{\text{TM}} \equiv \text{TE}$ , and

$$R_l^{\text{TM}} = -(R_l^{\text{TE}})^* \equiv 1 - \exp[-2i(\varphi_l^{\text{TM}} - \varphi_l^{\text{TE}})], \quad (\text{A23})$$

$$S_l^p \equiv 1 - \exp[-2i(\varphi_{l+1}^p - \varphi_l^p)]. \quad (\text{A24})$$

For better readability we have chosen to not specify explicitly that  $\bar{c}_{lmg}^p$  depends on  $(\theta_k, \phi_k)$  in the above expressions. This concludes the derivation of the coupling rates for spheres of arbitrary refractive index and size.

### Small-particle limit

Finally, let us explain how to derive the small-particle limit of the coupling rates, that is, Eq. (10). The small-particle limit  $\sqrt{\epsilon}kR \ll 1$  is obtained by realizing that, through  $R_l^p$  and  $S_l^p$ , the contribution of the individual terms of different  $l \in \mathbb{N}^+$  in Eq. (A19) to the total sum decreases exponentially with increasing  $l$ . For  $q \equiv kR \rightarrow 0$  we have  $R_l^p = O(q^{2l+1})$ ,  $S_l^{\text{TE}} = O(q^{2l+3})$ , and  $S_l^{\text{TM}} = O(q^{2l+1})$ . The leading-order terms read

$$R_1^{\text{TM}} \simeq R_1^{\text{TE}} \simeq -S_1^{\text{TM}} \simeq -\frac{4i}{3} \frac{\epsilon - 1}{\epsilon + 2} (kR)^3 = -\frac{i\alpha k^3}{3\pi\epsilon_0}, \quad (\text{A25})$$

where  $\alpha = 3\epsilon_0 V(\epsilon - 1)/(\epsilon + 2)$  is the polarizability of the dielectric sphere and  $V$  the volume of the sphere. Retaining only those terms (A19) directly leads to

$$g_{\kappa\kappa'\mu} \simeq \frac{ir_0\mu\alpha}{\epsilon_0} \frac{ckk'}{2(2\pi)^3} (\mathbf{e}_g^* \cdot \mathbf{e}_{g'})(\mathbf{e}_\kappa - \mathbf{e}_{\kappa'}) \cdot \mathbf{e}_\mu, \quad (\text{A26})$$

where  $\mathbf{e}_\kappa$  denotes the unit vector parallel to the wave vector  $\mathbf{k}$ . This expression agrees with the heuristically derived expressions for the coupling rates (see Sec. II).

## 2. Derivation of the transition amplitudes

In this section we consider Stokes and anti-Stokes scattering processes as shown in Fig. 1 and derive the corresponding transition amplitudes in first-order perturbation theory in the asymptotic limit [cf. Eq. (15)]. These processes describe the scattering of a single photon from a coherently populated tweezer mode into a mode  $\kappa$  (not excluding the tweezer mode) by generating or absorbing a center-of-mass phonon through the dynamics generated by the fundamental Hamiltonian  $\hat{H} = \hat{H}_0 + \hat{H}_{\text{int}}$  in Eq. (8).

The transition amplitudes for this processes read  $\tau_{\kappa\mu}^p(t, t') \equiv \langle \Psi_{\text{out}}^p | \hat{U}(t, t') | \Psi_{\text{in}} \rangle$ , with the input state  $|\Psi_{\text{in}}\rangle \equiv |n_x, n_y, n_z\rangle \otimes |\Psi_{\text{cl}}\rangle$  ( $n_\mu > 0$ ), the output states  $|\Psi_{\text{out}}^S\rangle \equiv \hat{a}_\kappa^\dagger \hat{b}_\mu^\dagger |\Psi_{\text{in}}\rangle$  and  $|\Psi_{\text{out}}^{\text{aS}}\rangle \equiv \hat{a}_\kappa^\dagger \hat{b}_\mu |\Psi_{\text{in}}\rangle$  describing Stokes ( $p = S$ ) and anti-Stokes ( $p = \text{aS}$ ) processes respectively, the time-evolution operator in the Schrödinger picture  $\hat{U}(t, t')$ , and  $|\Psi_{\text{cl}}\rangle = \mathcal{D}(\alpha_\kappa)|0\rangle_{\text{em}}$  as defined in Eq. (11) with the coherent and monochromatic amplitude  $\alpha_\kappa$  with frequency  $\omega_0$ . We rewrite the transition amplitude  $\tau_{\kappa\mu}^p$  with  $p \in \{S, \text{aS}\}$  as

$$\tau_{\kappa\mu}^S = \exp[-i(\omega_\kappa + \Omega_\mu)t] \langle \Psi_{\text{in}} | \exp(-i\hat{H}_0t/\hbar) \hat{a}_\kappa \hat{b}_\mu \hat{U}_{\text{int}}(t, t') \exp(i\hat{H}_0t'/\hbar) | \Psi_{\text{in}} \rangle, \quad (\text{A27})$$

$$\tau_{\kappa\mu}^{\text{aS}} = \exp[-i(\omega_\kappa - \Omega_\mu)t] \langle \Psi_{\text{in}} | \exp(-i\hat{H}_0t/\hbar) \hat{a}_\kappa \hat{b}_\mu^\dagger \hat{U}_{\text{int}}(t, t') \exp(i\hat{H}_0t'/\hbar) | \Psi_{\text{in}} \rangle, \quad (\text{A28})$$

where  $\hat{U}_{\text{int}}(t, t') \equiv \exp(i\hat{H}_0t/\hbar) \hat{U}(t, t') \exp(-i\hat{H}_0t'/\hbar)$  defines the time-evolution operator in the interaction picture.

In the regime where the coupling rates  $g_{\kappa\kappa'\mu}$  are smaller than the trap frequencies  $\Omega_\mu$ , we expand  $\hat{U}_{\text{int}}(t, t')$  up to first order in time-dependent perturbation theory and set  $t, t' = \pm T/2$ , namely,

$$\hat{U}_{\text{int}}(T/2, -T/2) \simeq 1 - \frac{i}{\hbar} \int_{-T/2}^{T/2} ds \exp(i\hat{H}_0 s) \hat{H}_{\text{int}} \exp(-i\hat{H}_0 s) \quad (\text{A29})$$

$$= 1 - 2i\pi \sum_{\kappa\kappa'\mu} g_{\kappa\kappa'\mu} \hat{a}_\kappa^\dagger \hat{a}_{\kappa'} [\hat{b}_\mu \delta_T(\omega_\kappa - \omega_{\kappa'} - \Omega_\mu) + \hat{b}_\mu^\dagger \delta_T(\omega_\kappa - \omega_{\kappa'} + \Omega_\mu)], \quad (\text{A30})$$

where  $\delta_T(\omega) \equiv (2\pi)^{-1} \int_{-T/2}^{T/2} ds \exp(i\omega s)$  defines a nascent delta function. This leads to

$$\begin{aligned} \tau_{\kappa\mu}^S &\simeq -2i\pi(n_\mu + 1) \exp\left(-i(\omega_\kappa + \Omega_\mu)T/2 - i \sum_v n_v \Omega_v T\right) \sum_{\kappa_1\kappa_2} g_{\kappa_1\kappa_2\mu} \\ &\times \langle \Psi_{\text{cl}} | \exp[-i\hat{H}_0 T/(2\hbar)] \hat{a}_\kappa \hat{a}_{\kappa_1}^\dagger \hat{a}_{\kappa_2} \exp[-i\hat{H}_0 T/(2\hbar)] | \Psi_{\text{cl}} \rangle \delta_T(\omega_{\kappa_1} - \omega_{\kappa_2} + \Omega_\mu), \end{aligned} \quad (\text{A31})$$

for the Stokes process and

$$\begin{aligned} \tau_{\kappa\mu}^{\text{aS}} &\simeq -2i\pi n_\mu \exp\left(-i(\omega_\kappa - \Omega_\mu)T/2 - i \sum_v n_v \Omega_v T\right) \sum_{\kappa_1\kappa_2} g_{\kappa_1\kappa_2\mu} \\ &\times \langle \Psi_{\text{cl}} | \exp[-i\hat{H}_0 T/(2\hbar)] \hat{a}_\kappa \hat{a}_{\kappa_1}^\dagger \hat{a}_{\kappa_2} \exp[-i\hat{H}_0 T/(2\hbar)] | \Psi_{\text{cl}} \rangle \delta_T(\omega_{\kappa_1} - \omega_{\kappa_2} - \Omega_\mu), \end{aligned} \quad (\text{A32})$$

for the anti-Stokes process, where we have used  $\hat{b}_\mu |n_\mu\rangle = \sqrt{n_\mu} |n_\mu - 1\rangle$  and  $\hat{b}_\mu^\dagger |n_\mu\rangle = \sqrt{n_\mu + 1} |n_\mu + 1\rangle$ . To further simplify the expression we use that  $\mathcal{D}^\dagger(\alpha_\kappa)\mathcal{D}(\alpha_\kappa) = 1$ ,  $\mathcal{D}^\dagger(\alpha_\kappa)a_\kappa\mathcal{D}(\alpha_\kappa) = \hat{a}_\kappa + \alpha_\kappa$ , and  $\hat{a}_\kappa|0\rangle_{\text{em}} = 0$ . This leads to

$$\begin{aligned} \sum_{\kappa_1\kappa_2} g_{\kappa_1\kappa_2\mu} \langle \Psi_{\text{cl}} | \exp[-i\hat{H}_0 T/(2\hbar)] \hat{a}_\kappa \hat{a}_{\kappa_1}^\dagger \hat{a}_{\kappa_2} \exp[-i\hat{H}_0 T/(2\hbar)] | \Psi_{\text{cl}} \rangle \delta_T(\omega_{\kappa_1} - \omega_{\kappa_2} \pm \Omega_\mu) \\ = \exp(-i\omega_0 T/2) \sum_{\kappa_1} G_{\kappa_1\mu} \langle \Psi_{\text{cl}} | \exp[-i\hat{H}_0 T/(2\hbar)] \hat{a}_\kappa \hat{a}_{\kappa_1}^\dagger \exp[-i\hat{H}_0 T/(2\hbar)] | \Psi_{\text{cl}} \rangle \delta_T(\omega_{\kappa_1} - \omega_0 \pm \Omega_\mu), \end{aligned} \quad (\text{A33})$$

where we have defined  $G_{\kappa\mu} \equiv \sum_{\kappa'} \alpha_{\kappa'} g_{\kappa\kappa'\mu}$ . Using  $[a_\kappa, a_{\kappa'}^\dagger] = \delta_{\kappa\kappa'}$  and  $\Omega_\mu > 0$ , we finally arrive at

$$\tau_{\kappa\mu}^S = -2i\pi(n_\mu + 1) \exp\left[-iT\left(\omega_0 + \sum_v n_v \Omega_v\right)\right] G_{\kappa\mu} \delta_T(\omega_\kappa - \omega_0 + \Omega_\mu) \langle \Psi_{\text{cl}} | \exp(-i\hat{H}_0 T/\hbar) | \Psi_{\text{cl}} \rangle, \quad (\text{A34})$$

$$\tau_{\kappa\mu}^{\text{aS}} = -2i\pi n_\mu \exp\left[-iT\left(\omega_0 + \sum_v n_v \Omega_v\right)\right] G_{\kappa\mu} \delta_T(\omega_\kappa - \omega_0 - \Omega_\mu) \langle \Psi_{\text{cl}} | \exp(-i\hat{H}_0 T/\hbar) | \Psi_{\text{cl}} \rangle. \quad (\text{A35})$$

### 3. Derivation of the IRPs and recoil heating rates

In this section we combine the results of the two preceding sections in order to derive explicit expressions for the recoil heating rates (19) and the information radiation patterns (22) associated with the center-of-mass motion along the  $\mu$  axis.

Using the transition amplitudes  $\tau_{\kappa\mu}^p$  in Eqs. (A34) and (A35), we can derive the transition probability rates in the asymptotic limit [76], namely,

$$\lim_{T \rightarrow \infty} \frac{\sum_\kappa |\tau_{\kappa\mu}^S|^2}{T} = (n_\mu + 1) \Gamma_\mu^+, \quad (\text{A36})$$

$$\lim_{T \rightarrow \infty} \frac{\sum_\kappa |\tau_{\kappa\mu}^{\text{aS}}|^2}{T} = n_\mu \Gamma_\mu^- \quad (\text{A37})$$

for Stokes ( $p = S$ ) and anti-Stokes ( $p = \text{aS}$ ) processes, respectively, and  $\Gamma_\mu^\pm \equiv 2\pi \sum_\kappa |G_{\kappa\mu}|^2 \delta(\omega_\kappa - \omega_0 \pm \Omega_\mu)$ . For coupling rates that are sufficiently broadband, i.e.,  $|\Gamma_\mu^+ - \Gamma_\mu^-| \ll \Gamma_\mu^+ + \Gamma_\mu^-$ , we define a single transition rate  $\Gamma_\mu = 2\pi \sum_\kappa |G_{\kappa\mu}|^2 \delta(\omega_\kappa - \omega_0)$ , which can be shown to correspond to the phonon heating rate due to laser recoil.

Inserting the expression for the linearized coupling rate  $G_{\kappa\mu}$ , we arrive at

$$\Gamma_\mu = 2\pi \sum_\kappa \left| \sum_{\kappa'} \alpha_{\kappa'} g_{\kappa\kappa'\mu} \right|^2 \delta(\omega_\kappa - \omega_0), \quad (\text{A38})$$

where  $\alpha_\kappa$  is the coherent amplitude of the monochromatic coherent state  $|\psi_{\text{cl}}\rangle$  [Eq. (11)] with frequency  $\omega_\kappa = \omega_0$ . Inserting Eq. (A19), we arrive at

$$\Gamma_\mu = \frac{cr_{0\mu}^2}{2\pi} \sum_{lmp} \sum_{l'm'p'} \left( \sum_g \int d\Omega_k \bar{c}_{lmg}^{p*}(\theta_k, \phi_k) \bar{c}_{l'm'g}^{p'}(\theta_k, \phi_k) \right) A_{lm}^{\mu p} (A_{l'm'}^{\mu p'})^*, \quad (\text{A39})$$

where we have defined  $A_{lm}^{\mu p} \equiv \sum_\kappa \alpha_\kappa a_{lm}^{\mu p}(\theta_k, \phi_k)$ . We can greatly simplify the expression (A39) by evaluating the expression in large parentheses. Inserting Eqs. (A2) and (A3), we have, e.g., for  $p = p' = \text{TE}$ , that

$$\sum_g \int d\Omega_k \bar{c}_{lmg}^{\text{TE}*}(\theta_k, \phi_k) \bar{c}_{l'm'g}^{\text{TE}'}(\theta_k, \phi_k) = (-i)^l i'^l \Theta(l - |m|) \Theta(l' - |m'|) \int d\Omega_k \mathbf{X}_l^m(\theta_k, \phi_k) \cdot \sum_g \mathbf{e}_g^*(\theta, \phi) \otimes \mathbf{e}_g(\theta, \phi) \cdot \mathbf{X}_{l'}^{m'*}(\theta_k, \phi_k) \quad (\text{A40})$$

$$= (-i)^l i'^l \Theta(l - |m|) \Theta(l' - |m'|) \int d\Omega_k \mathbf{X}_l^m(\theta_k, \phi_k) \cdot (\mathbb{1} - \mathbf{e}_r \otimes \mathbf{e}_r) \cdot \mathbf{X}_{l'}^{m'*}(\theta_k, \phi_k) \quad (\text{A41})$$

$$= (-i)^l i'^l \Theta(l - |m|) \Theta(l' - |m'|) \int d\Omega_k \mathbf{X}_l^m(\theta_k, \phi_k) \cdot \mathbf{X}_{l'}^{m'*}(\theta_k, \phi_k) = \Theta(l - |m|) \delta_{ll'} \delta_{mm'}. \quad (\text{A42})$$

To arrive at the third line we used the completeness relation of the unit vectors, where  $\otimes$  denotes the dyadic product; to arrive at the fourth line we used the fact that  $\mathbf{X}_l^m(\theta, \phi)$  has a vanishing radial component; and finally in the last step we have used the orthogonality condition of the vector spherical harmonics. Analogous derivations for all remaining combinations of  $p, p' \in \{\text{TE}, \text{TM}\}$  lead to

$$\sum_g \int d\Omega_k \bar{c}_{lmg}^{p*}(\theta_k, \phi_k) \bar{c}_{l'm'g}^{p'}(\theta_k, \phi_k) = \Theta(l - |m|) \delta_{ll'} \delta_{mm'} \delta_{pp'} \quad (\text{A43})$$

and hence

$$\Gamma_\mu = \frac{cr_{0\mu}^2}{2\pi} \sum_{lmp} \Theta(l - |m|) |A_{lm}^{\mu p}|^2, \quad (\text{A44})$$

where  $A_{lm}^{\mu p}$  depends, through  $\alpha_\kappa$ , on the particular state of the electromagnetic field.

The IRP  $\mathcal{I}_\mu^p(\theta_k, \phi_k)$  is defined as the normalized angular distribution of the transition probability rate in the asymptotic limit, namely,

$$\mathcal{I}_\mu^p(\theta_k, \phi_k) \equiv \frac{\lim_{T \rightarrow \infty} \int_0^\infty dk k^2 \sum_g |\tau_{\kappa\mu}^p|^2}{\lim_{T \rightarrow \infty} \sum_\kappa |\tau_{\kappa\mu}^p|^2}, \quad (\text{A45})$$

with  $\int d\Omega_k \mathcal{I}_\mu(\theta_k, \phi_k) = 1$ . Within the broadband coupling regime, we obtain  $\mathcal{I}_\mu(\theta_k, \phi_k) \equiv \mathcal{I}_\mu^S(\theta_k, \phi_k) = \mathcal{I}_\mu^{\text{as}}(\theta_k, \phi_k)$ . Inserting Eq. (A34) first and then Eq. (A19), it follows that the IRP reads

$$\begin{aligned} \mathcal{I}_\mu(\theta_k, \phi_k) &= \frac{\sum_g \int_0^\infty dk k^2 |G_{\kappa\mu}|^2 \delta(\omega_\kappa - \omega_0)}{\sum_\kappa |G_{\kappa\mu}|^2 \delta(\omega_\kappa - \omega_0)} \\ &= \frac{\sum_g |\sum_{lmp} \bar{c}_{lmg}^{p*}(\theta_k, \phi_k) A_{lm}^{\mu p}|^2}{\sum_{lmp} \Theta(l - |m|) |A_{lm}^{\mu p}|^2}. \end{aligned} \quad (\text{A46})$$

## APPENDIX B: FOCUSED GAUSSIAN BEAM AS A LINEAR COMBINATION OF PLANE WAVES

Both central quantities of this article, namely, the recoil heating rate in Eq. (19) and the information radiation pattern in Eq. (22), crucially depend on the coherent amplitude  $\alpha_\kappa$  that specifies the particular state of the electromagnetic field. In this Appendix we derive an explicit expression for  $\alpha_\kappa$  for a single focused Gaussian beam and a standing-wave configuration of two counterpropagating focused Gaussian beams with an arbitrary phase shift.

Let us start by deriving a general expression for the electric field in the focal region of an aplanatic lens, i.e., a lens designed to minimize chromatic aberrations. We can then use this expression to infer  $\alpha_\kappa$  through Eq. (12). We consider a monochromatic incoming field  $\mathbf{E}_{\text{in}}(\mathbf{r}, t) \equiv \mathbf{E}_{\text{in}}(\mathbf{r}) \exp(-i\omega_0 t) + \text{c.c.}$  of frequency  $\omega_0$  and wavelength  $\lambda_0 = 2\pi c/\omega_0$ . The aplanatic lens is characterized by its focal length  $f$  and numerical aperture  $\text{NA} = \sin \theta_{\text{NA}}$ . Note that the evanescent components of the incident electric field make a negligible contribution to the focal field given that  $f \gg \lambda_0$ . Using this approximation, we can show shown that the electric field in the focal region reads [72,101]

$$\begin{aligned} \mathbf{E}(\mathbf{r}) &= \frac{k_0 f}{2\pi i} \int_{\mathcal{D}_\pm} d\Omega_k \mathbf{E}_\infty^\pm(f, \theta_k, \phi_k) \exp[ikr \cos \theta_k \cos \theta \\ &\quad + ikr \sin \theta_k \sin \theta \cos(\phi_k - \phi)], \end{aligned} \quad (\text{B1})$$

where

$$\begin{aligned} \mathbf{E}_\infty^\pm(f, \theta_k, \phi_k) &= \sqrt{|\cos \theta_k|} [\mathbf{E}_{\text{in}}(f, \theta_k, \phi_k) \cdot \mathbf{e}_\phi(\theta_k, \phi_k)] \mathbf{e}_\phi(\theta_k, \phi_k) \\ &\quad \pm \sqrt{|\cos \theta_k|} [\mathbf{E}_{\text{in}}(f, \theta_k, \phi_k) \cdot \mathbf{e}_\rho(\theta_k, \phi_k)] \mathbf{e}_\rho(\theta_k, \phi_k) \end{aligned} \quad (\text{B2})$$

is the far-field angular spectrum of the refracted for an incoming field propagating along the positive (+) or negative (-)  $z$  axis and  $\mathbf{e}_\phi$  and  $\mathbf{e}_\rho$  denote the unit vectors of the corresponding cylindrical coordinate system. The

corresponding integration domains depend on the numerical aperture and read  $\mathcal{D}_+ = \{\theta_k, \phi_k \in \mathbb{R} \mid 0 \leq \theta_k \leq \theta_{\text{NA}}, 0 \leq \phi_k < 2\pi\}$  and  $\mathcal{D}_- = \{\theta_k, \phi_k \in \mathbb{R} \mid \pi - \theta_{\text{NA}} \leq \theta_k \leq \pi, 0 \leq \phi_k < 2\pi\}$ . Note that Eq. (B2) is derived on the premise that, upon refraction by the lens, the energy of the field is conserved and that the angle between the polarization and propagation of the field remains constant.

Inserting Eq. (B2) in Eq. (B1), we immediately see that we can write  $\mathbf{E}(\mathbf{r}) = i \sum_{\kappa} \sqrt{\hbar \omega_{\kappa} / 2 \epsilon_0} \alpha_{\kappa} \mathbf{G}_{\kappa}(\mathbf{r})$  with the normalized plane-wave mode  $\mathbf{G}_{\kappa}(\mathbf{r}) = \exp(i\mathbf{k} \cdot \mathbf{r}) \mathbf{e}_g / (2\pi)^{3/2}$ . Thus, the focused field  $\mathbf{E}(\mathbf{r})$  is given by a linear combination of plane waves with coefficients that depend on the angular spectrum and the propagation direction ( $\pm$ ) of the incoming beam, namely,

$$\alpha_1^{\pm}(k, \theta_k, \phi_k) = -i \sqrt{\frac{4\pi\epsilon_0}{\hbar\omega_0}} k_0 f \sqrt{|\cos \theta_k|} [\mathbf{E}_{\text{in}}(f, \theta_k, \phi_k) \cdot \mathbf{e}_{\phi}(\theta_k, \phi_k)] \frac{\delta(k - k_0)}{k_0^2}, \quad (\text{B3})$$

$$\alpha_2^{\pm}(k, \theta_k, \phi_k) = \pm \sqrt{\frac{4\pi\epsilon_0}{\hbar\omega_0}} k_0 f \sqrt{|\cos \theta_k|} [\mathbf{E}_{\text{in}}(f, \theta_k, \phi_k) \cdot \mathbf{e}_{\rho}(\theta_k, \phi_k)] \frac{\delta(k - k_0)}{k_0^2}, \quad (\text{B4})$$

where  $k_0 \equiv \omega_0/c$ . Note that in the presence of a dielectric sphere of arbitrary refractive index and size, the focused fields are obtained by simply replacing the plane-wave modes  $\mathbf{G}_{\kappa}(\mathbf{r})$  by the scattering eigenmodes  $\mathbf{F}_{\kappa}(\mathbf{r})$  [58], that is,  $\mathbf{E}(\mathbf{r}) = i \sum_{\kappa} \sqrt{\hbar \omega_{\kappa} / 2 \epsilon_0} \alpha_{\kappa} \mathbf{F}_{\kappa}(\mathbf{r})$ .

Having derived a general expression for the focal field, let us now consider a single incoming  $x$ -polarized paraxial Gaussian beam of waist  $w_0$  propagating along the positive or negative  $z$  axis, that is,  $\mathbf{E}_{\text{in}}(f, \theta_k, \phi_k) = E_0 \exp(-f^2 \sin^2 \theta_k / w_0^2) \mathbf{e}_x$ . This leads to

$$\alpha_1^{\pm}(k, \theta_k, \phi_k) = \sqrt{\frac{4\pi\epsilon_0}{\hbar\omega_0}} k_0 f E_0 \sqrt{|\cos \theta_k|} \times \exp(-f^2 \sin^2 \theta_k / w_0^2) i \sin \phi_k \frac{\delta(k - k_0)}{k_0^2}, \quad (\text{B5})$$

$$\alpha_2^{\pm}(k, \theta_k, \phi_k) = \pm \sqrt{\frac{4\pi\epsilon_0}{\hbar\omega_0}} k_0 f E_0 \sqrt{|\cos \theta_k|} \times \exp(-f^2 \sin^2 \theta_k / w_0^2) \cos \phi_k \frac{\delta(k - k_0)}{k_0^2}. \quad (\text{B6})$$

The coherent amplitude enters in the expressions for the recoil heating rate and IRP through  $A_{lm\pm}^{\mu p} = \sum_{\kappa} \alpha_{\kappa}^{\pm} c_{lm\kappa}^{\mu p}(\theta_k, \phi_k)$ . The Dirac delta in  $k - k_0$  renders the integration over  $k$  trivial and we only need to evaluate the sum over the polarizations  $g$  and the integral over the angles  $\theta_k$  and  $\phi_k$ . One can see in Eqs. (A20)–(A22) that the only quantity that depends on these variables is  $\tilde{c}_{lm\kappa}^p(\theta_k, \phi_k)$ . In order to further simplify the computation of the recoil heating rate and IRP, let us therefore derive an explicit expression for  $C_{lm\pm}^p \equiv \sum_{\kappa} \alpha_{\kappa}^{\pm} c_{lm\kappa}^p(\theta_k, \phi_k)$ . With this quantity we immediately obtain an expressions for

$A_{lm\pm}^{\mu p}$  by replacing  $\tilde{c}_{lm\kappa}^p(\theta_k, \phi_k)$  by  $C_{lm\kappa}^p$  in Eqs. (A20)–(A22). Inserting Eqs. (A2) and (A3) in  $C_{lm\pm}^p \equiv \sum_{\kappa} \alpha_{\kappa}^{\pm} c_{lm\kappa}^p(\theta_k, \phi_k)$ , we have

$$C_{lm+}^{\text{TE}} = i^l \Theta(l - |m|) k_0 f E_0 \sqrt{\frac{4\pi\epsilon_0}{\hbar\omega_0}} \int_{\mathcal{D}_+} d\Omega_k \sqrt{|\cos \theta_k|} \times \exp(-f^2 \sin^2 \theta_k / w_0^2) \mathbf{X}_l^{m*}(\theta_k, \phi_k) \cdot (-\sin \phi_k \mathbf{e}_{\phi} + \cos \phi_k \mathbf{e}_{\theta}), \quad (\text{B7})$$

$$C_{lm+}^{\text{TM}} = i^l \Theta(l - |m|) k_0 f E_0 \sqrt{\frac{4\pi\epsilon_0}{\hbar\omega_0}} \int_{\mathcal{D}_+} d\Omega_k \sqrt{|\cos \theta_k|} \times \exp(-f^2 \sin^2 \theta_k / w_0^2) \mathbf{X}_l^{m*}(\theta_k, \phi_k) \cdot (\sin \phi_k \mathbf{e}_{\theta} + \cos \phi_k \mathbf{e}_{\phi}). \quad (\text{B8})$$

Integration over  $\phi_k$  can be performed analytically and leads to

$$C_{lm+}^p = i^l k_0 f E_0 \sqrt{\frac{4\pi^3\epsilon_0}{\hbar\omega_0}} (\mathbf{Z}_{lm} \cdot \mathbf{u}_+^p \delta_{m1} + \mathbf{Z}_{lm} \cdot \mathbf{u}_+^{*p} \delta_{m-1}), \quad (\text{B9})$$

where we have defined the two vectors  $\mathbf{u}_+^{\text{TE}} \equiv \mathbf{e}_{\theta} + i\mathbf{e}_{\phi}$  and  $\mathbf{u}_+^{\text{TM}} \equiv \mathbf{e}_{\phi} - i\mathbf{e}_{\theta}$  and

$$\mathbf{Z}_{lm} \equiv \Theta(l - |m|) \int_0^{\theta_{\text{NA}}} d\theta \sin \theta \sqrt{|\cos \theta|} \times \exp(-f^2 \sin^2 \theta / w_0^2) \mathbf{X}_l^{m*}(\theta, 0). \quad (\text{B10})$$

Analogously, using  $\mathbf{X}_l^{\pm 1}(\pi - \theta_k, 0) = (-1)^{l+1} [\mathbf{X}_l^{\pm 1}(\theta_k, 0)]^*$ , we obtain

$$C_{lm-}^p = -(-i)^l k_0 f E_0 \sqrt{\frac{4\pi^3\epsilon_0}{\hbar\omega_0}} (\mathbf{Z}_{lm}^* \cdot \mathbf{u}_-^p \delta_{m1} + \mathbf{Z}_{lm}^* \cdot \mathbf{u}_-^{*p} \delta_{m-1}), \quad (\text{B11})$$

where we have defined  $\mathbf{u}_-^{\text{TE}} \equiv -\mathbf{e}_{\theta} + i\mathbf{e}_{\phi}$  and  $\mathbf{u}_-^{\text{TM}} \equiv -\mathbf{e}_{\phi} - i\mathbf{e}_{\theta}$ . We have now derived an expression for  $C_{lm\pm}^p$  in the case of focused Gaussian beams propagating along the positive (+) or negative (−)  $z$  axis. For the standing-wave configuration we combine both beams with a relative phase  $\Phi$ , which leads to

$$\tilde{C}_{lm}^p(\Phi) \equiv C_{lm+}^p + \exp(i\Phi) C_{lm-}^p, \quad (\text{B12})$$

where the intensity at the focus scales as  $\cos^2(\Phi/2)$  with the relative phase.

## 1. Characterization of the focused field

Note that we can relate the electric field amplitude  $E_0$  to the power  $P$  that passes through a single lens, that is,

$$P = 2\mu_0^{-1} f^2 \int_{\mathcal{D}} d\Omega_k [\mathbf{E}_{\infty}(f, \theta_k, \phi_k) \mathbf{B}_{\infty}^*(f, \theta_k, \phi_k)] \cdot \mathbf{e}_r(\theta_k, \phi_k) = \epsilon_0 c E_0^2 \pi w^2 [1 - \exp(-2f^2 \sin^2 \theta_{\text{NA}} / w_0^2)], \quad (\text{B13})$$

where  $\mu_0$  denotes the vacuum permeability and  $\mathbf{B}(\mathbf{r}, t) = \mathbf{B}(\mathbf{r}) \exp(-i\omega_0 t) + \text{c.c.}$  defines the magnetic field. In order to achieve maximum focusing one needs to overfill the lens, that is,  $f_0 \gg 1$  with filling factor  $f_0 \equiv w_0/(f \sin \theta_{\text{NA}})$ . In this case we can approximate  $P \simeq 2\pi\epsilon_0 c(f E_0)^2 \sin^2 \theta_{\text{NA}}$ . Throughout the article we consider a filling factor  $f_0 = 10$ .

Let us now derive how the waist of the focused Gaussian beam depends on the numerical aperture of the overfilled lens. Using the electric and magnetic fields in the focal region [72], we calculate, similarly to Eq. (B13), the power that passes through a circular aperture with radius  $a$  centered at the focal point and oriented perpendicular to the  $z$  axis, that is,

$$P(a) = 2\mu_0^{-1} \int_0^a d\rho \rho \int_0^{2\pi} d\phi [\mathbf{E}(\rho, \phi, 0) \times \mathbf{B}^*(\rho, \phi, 0)] \cdot \mathbf{e}_z. \quad (\text{B14})$$

Analogously to a Gaussian beam, we define the waist  $w$  of a focused Gaussian beam as the radius of the circular aperture for which  $P(w) = [1 - \exp(-2)] \lim_{a \rightarrow \infty} P(a)$ , that is, 86% of the total power is transmitted through that aperture of radius  $w$ . In Fig. 2(b) we show  $w/\lambda_0$  for numerical apertures  $\text{NA} \geq 0.1$  and a single Gaussian beam. As expected, the waist decreases rapidly with increasing numerical aperture and reaches a value on the order of the wavelength  $\lambda_0$ , which corresponds to the diffraction limit [72].

### APPENDIX C: FABRY-PÉROT INTERFEROMETER

In this Appendix we provide a simple model for the recoil localization parameter and the IRP for lenses of numerical apertures  $\text{NA} \geq 0.75$  and dielectric spheres or radius  $R > \lambda_0$ . For these large numerical apertures the waist of the focused Gaussian beam is smaller than the wavelength [see Fig. 2(b)]. It follows that the system can be modeled by a collimated beam that is normally incident on a dielectric slab of thickness  $D \equiv 2R$  and relative permittivity  $\epsilon$ , i.e., a Fabry-Pérot interferometer. In the following we derive both the recoil localization parameter and the IRP for the subspace of two  $x$ -polarized scattering eigenmodes propagating perpendicular to the slab. These modes are given by  $\mathbf{f}_k^\sigma(\mathbf{r}) = A_k^\sigma f_k^p(z)\mathbf{e}_x$ , for  $\sigma = L, R$ , with normalization constant  $A_k^\sigma$ , eigenfrequency  $\omega_k^\sigma = ck$ , and

$$f_k^L(z) = \exp(ikz + i\Phi) + r \exp(-ikz + i\Phi) \quad \text{for } z < -D/2, \quad (\text{C1})$$

$$f_k^L(z) = t \exp(ikz + i\Phi) \quad \text{for } z > D/2, \quad (\text{C2})$$

$$f_k^R(z) = t \exp(-ikz) \quad \text{for } z < -D/2, \quad (\text{C3})$$

$$f_k^R(z) = \exp(-ikz) + r \exp(ikz) \quad \text{for } z > D/2. \quad (\text{C4})$$

Here  $\Phi$  is a relative phase between the  $L$  and  $R$  modes. The reflection and transmission coefficients are given by

$$r = \frac{(1 - \epsilon) \sin(\sqrt{\epsilon}q)}{(\epsilon + 1) \sin(\sqrt{\epsilon}q) + 2i\sqrt{\epsilon} \cos(\sqrt{\epsilon}q)}, \quad (\text{C5})$$

$$t = \frac{2i\sqrt{\epsilon}}{(\epsilon + 1) \sin(\sqrt{\epsilon}q) + 2i\sqrt{\epsilon} \cos(\sqrt{\epsilon}q)}, \quad (\text{C6})$$

where  $q \equiv kD$ . The coupling rates  $g_{\sigma\sigma'}$  are determined, analogously to the main text, via the radiation pressure operator [see Eq. (5)]. Due to the simple geometry, they can readily be shown to read

$$g_{LL} \propto |r|^2, \quad (\text{C7})$$

$$g_{LR} \propto -i|r|^2 \text{Im}(t/r) \exp(i\Phi), \quad (\text{C8})$$

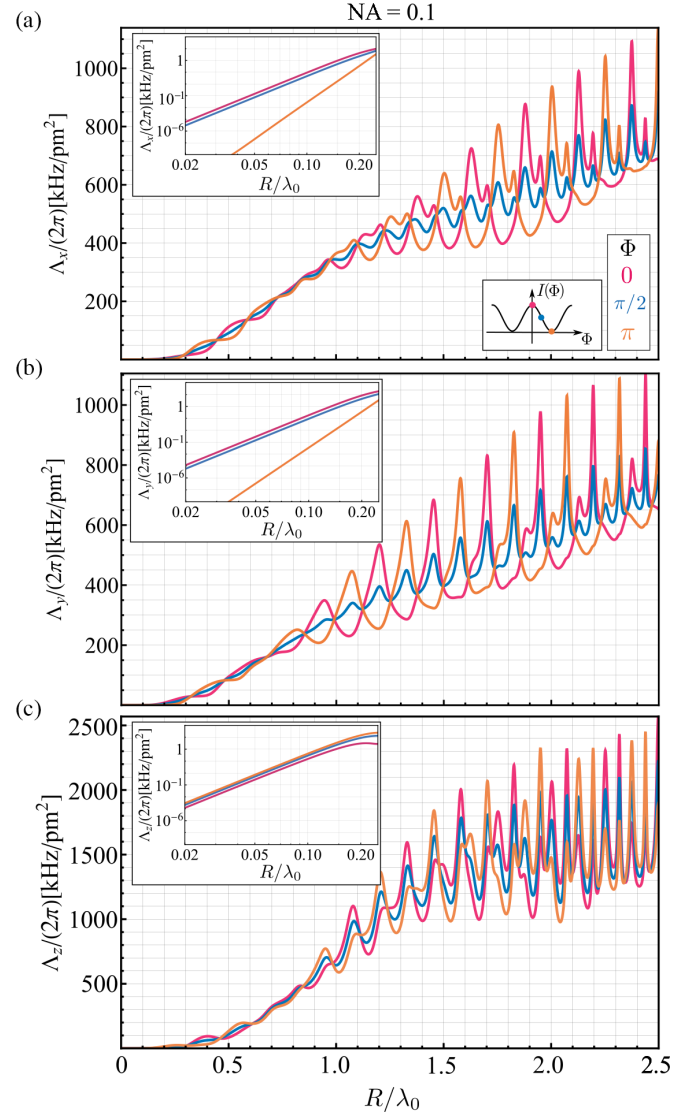


FIG. 9. Recoil localization parameter  $\Lambda_\mu = \Gamma_\mu/r_0^2$  for two focused  $x$ -polarized Gaussian beams counterpropagating along the  $z$  axis as a function of the silica sphere's radius  $R/\lambda_0$  for all three axes (a)  $\mu = x$ , (b)  $\mu = y$ , and (c)  $\mu = z$ . The values for the power, wavelength, and relative permittivity are listed in Table I. Each panel shows the recoil localization parameter for  $\Phi = 0, \pi/2, \pi$ ,  $\text{NA} = 0.10$ , and an inset with a detailed view of the small-particle regime for all three relative phases on a log-log plot. The inset in (a) maps the relative phase  $\Phi$  to the corresponding intensity at the origin.

$$g_{RL} \propto i|r|^2 \text{Im}(t/r) \exp(-i\Phi), \quad (\text{C9})$$

$$g_{RR} \propto -|r|^2. \quad (\text{C10})$$

First, let us assume the scenario where the  $L$  mode is in a coherent state. In the absence of the slab this corresponds to a plane wave propagating along the positive- $z$  axis. It follows that the recoil heating rate reads

$$\begin{aligned} \Gamma &\propto \sum_\sigma |g_{L\sigma}|^2 = |g_{LL}|^2 + |g_{LR}|^2 \\ &= |r|^4 \{1 + [\text{Im}(t/r)]^2\} = g_0^2 |r|^2. \end{aligned} \quad (\text{C11})$$

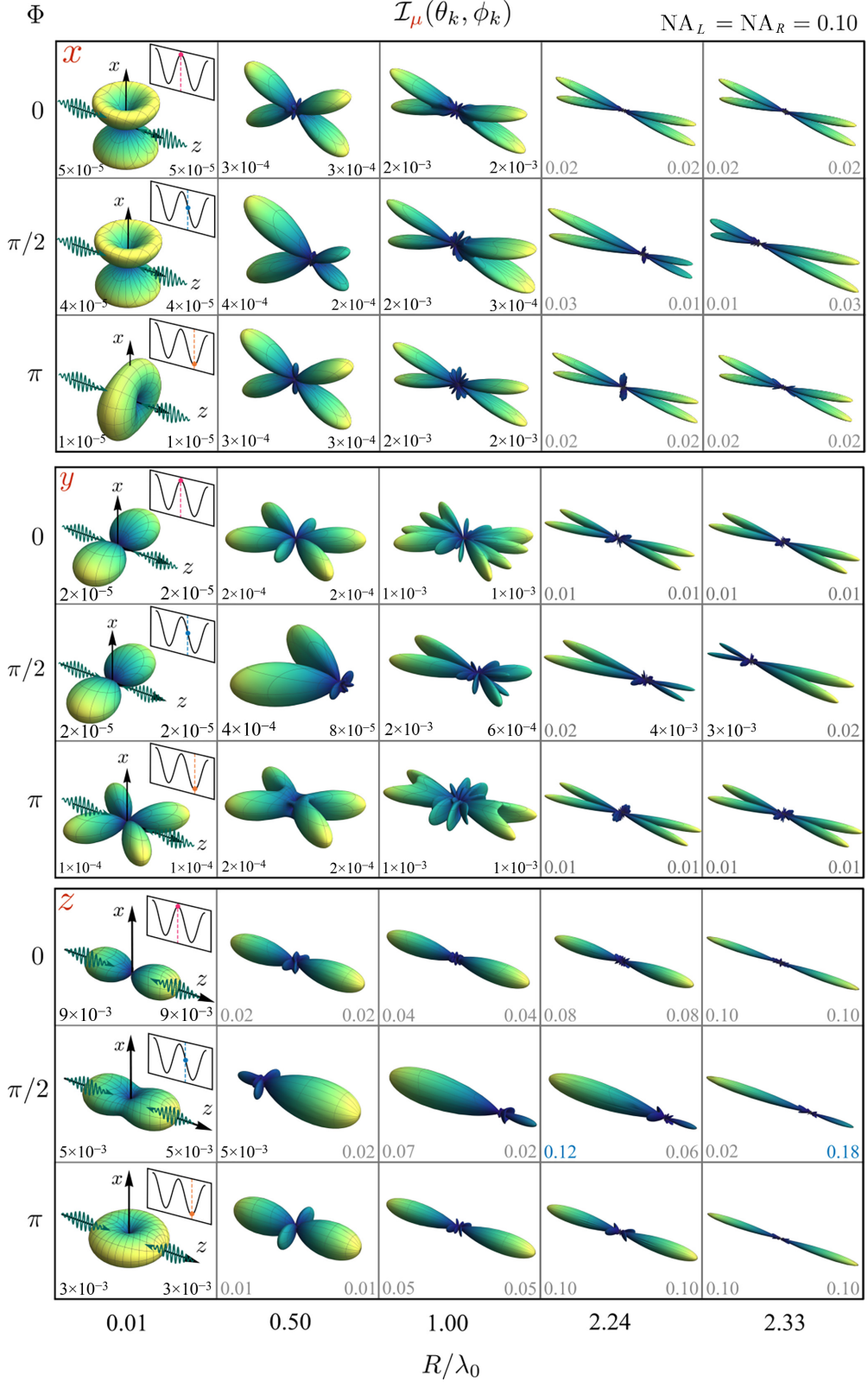


FIG. 10. Information radiation patterns  $\mathcal{I}_z(\theta_k, \phi_k)$  of a silica sphere, two focused  $x$ -polarized Gaussian beams counterpropagating parallel to the  $z$  axis (reference frame in the first row), and relative phases  $\Phi = 0, \pi/2, \pi$ . The value of the IRP is encoded in both the radial distance from the center and the color scale. The two focusing lenses have a numerical aperture  $\text{NA}_L = \text{NA}_R = 0.10$ . The detection efficiencies for the left and right lenses are shown in each panel (highlighted in blue for  $\eta_\mu^d > \frac{1}{9}$ ). Across the panels the value of  $R/\lambda_0$  is, for each column, constant and indicated below the last row.

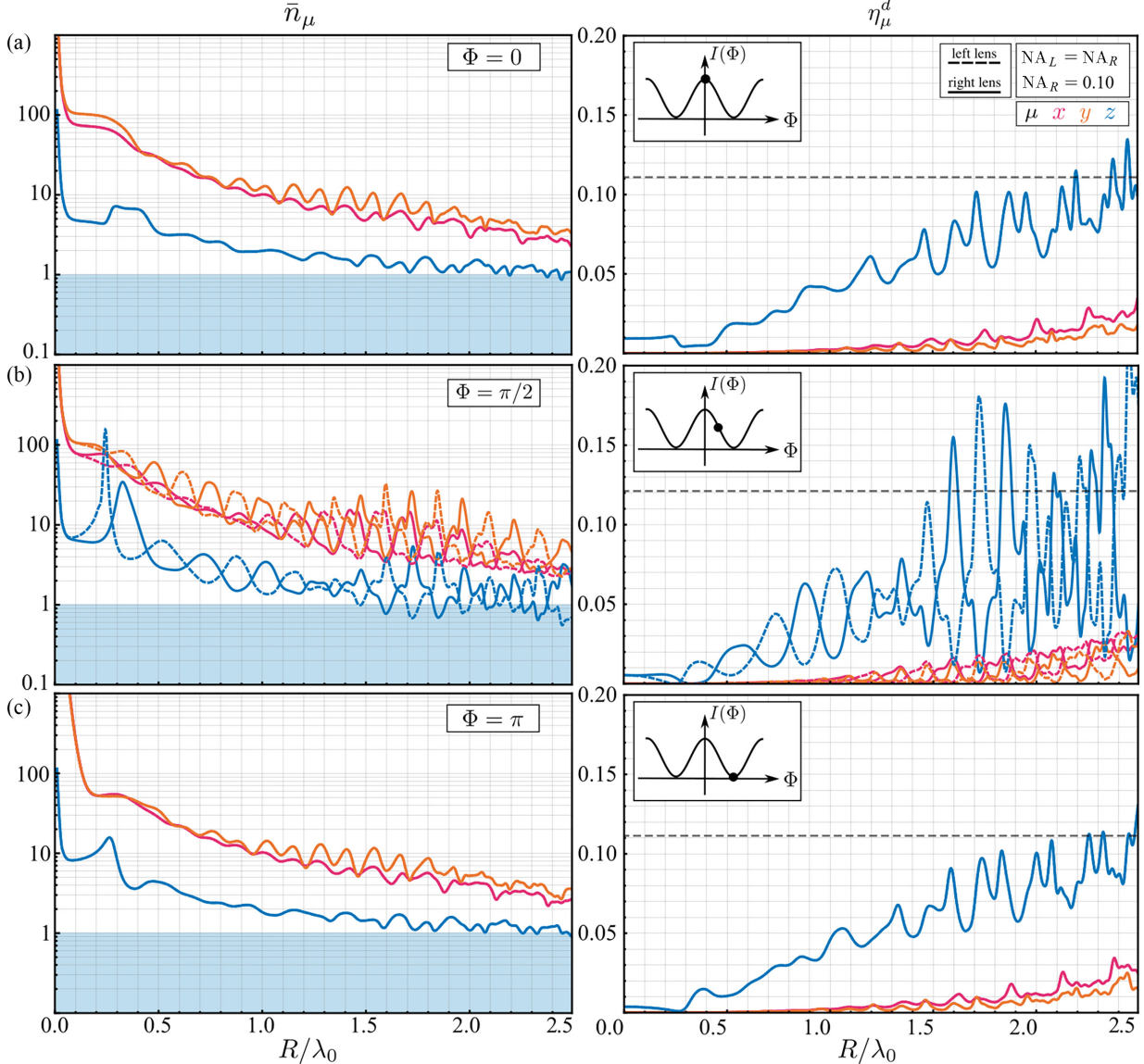


FIG. 11. Detection efficiencies  $\eta_\mu^d$  and minimum achievable mean phonon occupation number  $\bar{n}_\mu$  along  $x$ ,  $y$ , and  $z$  for ideal feedback as a function of  $R/\lambda_0$  for  $p = 10^{-9}$  mbar and  $T = 300$  K, at the same optical configuration as in Fig. 9, for (a)  $\Phi = 0$ , (b)  $\Phi = \pi/2$ , and (c)  $\Phi = \pi$  with an inset that maps the relative phase  $\Phi$  to the corresponding intensity at the origin. The dashed (solid) lines correspond to the values at the left (right) lens. The blue shaded area highlights the region where  $\bar{n}_\mu < 1$  and the gray dashed line shows  $\eta_\mu^d = \frac{1}{9}$ .

The  $\Gamma$  is maximal when the reflectance  $|r|^2$  is maximal, which happens periodically at  $\sqrt{\epsilon}q = \pi/2 + n\pi$ , with  $n \in \mathbb{N}_0$ . Note that these maxima also coincide with a maximal number of backscattered photons.

Second, let us assume that both the  $L$  and  $R$  modes are in a coherent state. In the absence of the slab this corresponds to a standing wave with an intensity  $\cos^2(\Phi/2)$  at the origin. It follows that the recoil heating rate reads

$$\Gamma \propto \sum_{\sigma} |g_{L\sigma} + g_{R\sigma}|^2 = |g_{LL} + g_{RL}|^2 + |g_{LR} + g_{RR}|^2. \quad (\text{C12})$$

Inserting the coupling rates, one immediately obtains that the two terms, which represent a left-oriented IRP and a right-

oriented IRP, respectively, are equal up to an interference term proportional to  $\pm \sin \Phi$ , namely,

$$|g_{LL} + g_{RL}|^2 = |r|^2 + 2|r|^4 \text{Im}(t/r) \sin \Phi, \quad (\text{C13})$$

$$|g_{LR} + g_{RR}|^2 = |r|^2 - 2|r|^4 \text{Im}(t/r) \sin \Phi. \quad (\text{C14})$$

Therefore, the recoil heating rate, which is obtained by summing over the two terms, i.e.,  $\Gamma \propto 2|r|^2$ , does not depend on  $\Phi$ . Furthermore, the left-oriented IRP and right-oriented IRP are only different for  $\Phi \neq 0, \pi$  and they oscillate from left to right as a function of  $D$ .

#### APPENDIX D: FIGURES

This Appendix contains Figs. 6, 7, and 8 for  $\text{NA}_L = \text{NA}_R = 0.1$ , shown respectively in Figs. 9, 10, and 11. For

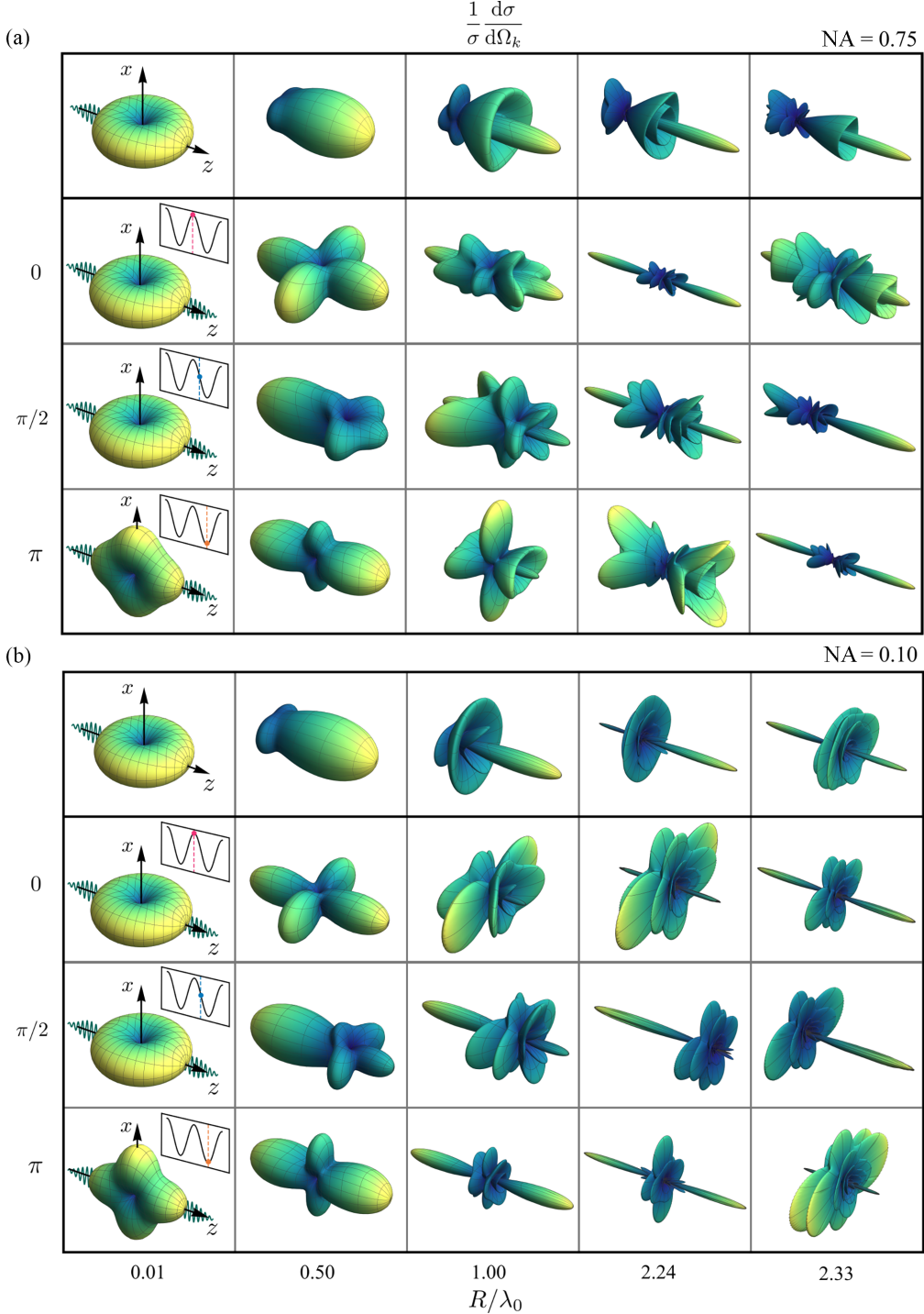


FIG. 12. Normalized Lorenz-Mie differential scattering cross section  $\sigma^{-1} d\sigma/d\Omega_k$  as a function of the radius for all optical configuration under consideration in the main text, i.e., the running- and standing-wave setups with low- and high-NA lenses, and relative phase  $\Phi = 0, \pi/2, \pi$ . The value of the differential scattering cross section is encoded in both the radial distance from the center and the color scale. Across the panels the value of  $R/\lambda_0$  is, for each column, constant and indicated below the last row.

the low-NA standing-wave configuration the simple one-dimensional model based on the Fabry-Pérot interferometer (see Appendix C) does not hold and the IRPs again become increasingly sharply peaked in the forward direction as the radius increases. In contrast to the running-wave configuration in Sec. IV C, the low-NA lenses lead to a much smaller detection efficiency which does not allow for ground-state cooling

for almost all axes, relative phases, and radii under consideration. Note, however, that  $\bar{n}_\mu \simeq 10$  appears to be feasible for large enough spheres.

For completeness, we also show the normalized Lorenz-Mie differential scattering cross section  $\sigma^{-1} d\sigma/d\Omega_k$  [100] for all optical configurations discussed in this work in Fig. 12.

- [1] L. Lorenz, Lysbevægelsen i og uden for en af plane lysbølger belyst kugle, *K. Dan. Vidensk. Selsk. Skr.* **6**, 1 (1890).
- [2] G. Mie, Beiträge zur optik trüber medien, speziell kolloidaler metallösungen, *Ann. Phys. (Leipzig)* **330**, 377 (1908).
- [3] A. Ashkin, Acceleration and Trapping of Particles by Radiation Pressure, *Phys. Rev. Lett.* **24**, 156 (1970).
- [4] A. Ashkin and J. M. Dziedzic, Optical levitation by radiation pressure, *Appl. Phys. Lett.* **19**, 283 (1971).
- [5] A. Ashkin and J. M. Dziedzic, Optical levitation in high vacuum, *Appl. Phys. Lett.* **28**, 333 (1976).
- [6] A. Ashkin, *Optical Trapping and Manipulation of Neutral Particles Using Lasers* (World Scientific, Singapore, 2006).
- [7] C. Gonzalez-Ballester, M. Aspelmeyer, L. Novotny, R. Quidant, and O. Romero-Isart, Levitodynamics: Levitation and control of microscopic objects in vacuum, *Science* **374**, eabg3027 (2021).
- [8] J. Millen, T. S. Monteiro, R. Pettit, and A. N. Vamivakas, Optomechanics with levitated particles, *Rep. Prog. Phys.* **83**, 026401 (2020).
- [9] U. Delić, M. Reisenbauer, K. Dare, D. Grass, V. Vuletić, N. Kiesel, and M. Aspelmeyer, Cooling of a levitated nanoparticle to the motional quantum ground state, *Science* **367**, 892 (2020).
- [10] A. Ranfagni, K. Børkje, F. Marino, and F. Marin, Two-dimensional quantum motion of a levitated nanosphere, *Phys. Rev. Res.* **4**, 033051 (2022).
- [11] J. Piotrowski, D. Windey, J. Vijayan, C. Gonzalez-Ballester, A. d. I. R. Sommer, N. Meyer, R. Quidant, O. Romero-Isart, R. Reimann, and L. Novotny, Simultaneous ground-state cooling of two mechanical modes of a levitated nanoparticle, *Nat. Phys.* **19**, 1009 (2023).
- [12] L. Magrini, P. Rosenzweig, C. Bach, A. Deutschmann-Olek, S. G. Hofer, S. Hong, N. Kiesel, A. Kugi, and M. Aspelmeyer, Real-time optimal quantum control of mechanical motion at room temperature, *Nature (London)* **595**, 373 (2021).
- [13] F. Tebbenjohanns, M. L. Mattana, M. Rossi, M. Frimmer, and L. Novotny, Quantum control of a nanoparticle optically levitated in cryogenic free space, *Nature (London)* **595**, 378 (2021).
- [14] M. Kamba, R. Shimizu, and K. Aikawa, Optical cold damping of neutral nanoparticles near the ground state in an optical lattice, *Opt. Express* **30**, 26716 (2022).
- [15] O. Romero-Isart, M. L. Juan, R. Quidant, and J. I. Cirac, Toward quantum superposition of living organisms, *New J. Phys.* **12**, 033015 (2010).
- [16] D. E. Chang, C. A. Regal, S. B. Papp, D. J. Wilson, J. Ye, O. Painter, H. J. Kimble, and P. Zoller, Cavity opto-mechanics using an optically levitated nanosphere, *Proc. Natl. Acad. Sci. USA* **107**, 1005 (2010).
- [17] O. Romero-Isart, A. C. Pflanzer, M. L. Juan, R. Quidant, N. Kiesel, M. Aspelmeyer, and J. I. Cirac, Optically levitating dielectrics in the quantum regime: Theory and protocols, *Phys. Rev. A* **83**, 013803 (2011).
- [18] B. Rodenburg, L. P. Neukirch, A. N. Vamivakas, and M. Bhattacharya, Quantum model of cooling and force sensing with an optically trapped nanoparticle, *Optica* **3**, 318 (2016).
- [19] F. Teffenjohanns, M. Frimmer, and L. Novotny, Optimal position detection of a dipolar scatterer in a focused field, *Phys. Rev. A* **100**, 043821 (2019).
- [20] C. Gonzalez-Ballester, P. Maurer, D. Windey, L. Novotny, R. Reimann, and O. Romero-Isart, Theory for cavity cooling of levitated nanoparticles via coherent scattering: Master equation approach, *Phys. Rev. A* **100**, 013805 (2019).
- [21] H. Rudolph, J. Schäfer, B. A. Stickler, and K. Hornberger, Theory of nanoparticle cooling by elliptic coherent scattering, *Phys. Rev. A* **103**, 043514 (2021).
- [22] M. Toroš, U. Delić, F. Hales, and T. S. Monteiro, Coherent-scattering two-dimensional cooling in levitated cavity optomechanics, *Phys. Rev. Res.* **3**, 023071 (2021).
- [23] A. C. Pflanzer, O. Romero-Isart, and J. I. Cirac, Master-equation approach to optomechanics with arbitrary dielectrics, *Phys. Rev. A* **86**, 013802 (2012).
- [24] T. Seberson and F. Robicheaux, Distribution of laser shot-noise energy delivered to a levitated nanoparticle, *Phys. Rev. A* **102**, 033505 (2020).
- [25] F. Teffenjohanns, M. Frimmer, A. Militaru, V. Jain, and L. Novotny, Cold Damping of an Optically Levitated Nanoparticle to Microkelvin Temperatures, *Phys. Rev. Lett.* **122**, 223601 (2019).
- [26] G. P. Conangla, F. Ricci, M. T. Cuairan, A. W. Schell, N. Meyer, and R. Quidant, Optimal Feedback Cooling of a Charged Levitated Nanoparticle with Adaptive Control, *Phys. Rev. Lett.* **122**, 223602 (2019).
- [27] M. A. Ciampini, T. Wenzl, M. Konopik, G. Thalhammer, M. Aspelmeyer, E. Lutz, and N. Kiesel, Experimental nonequilibrium memory erasure beyond Landauer's bound, *arXiv:2107.04429*.
- [28] M. Kamba, H. Kiuchi, T. Yotsuya, and K. Aikawa, Recoil-limited feedback cooling of single nanoparticles near the ground state in an optical lattice, *Phys. Rev. A* **103**, L051701 (2021).
- [29] A. Ashkin and J. M. Dziedzic, Feedback stabilization of optically levitated particles, *Appl. Phys. Lett.* **30**, 202 (1977).
- [30] T. Li, S. Kheifets, and M. G. Raizen, Millikelvin cooling of an optically trapped microsphere in vacuum, *Nat. Phys.* **7**, 527 (2011).
- [31] C. P. Blakemore, A. D. Rider, S. Roy, Q. Wang, A. Kawasaki, and G. Gratta, Three-dimensional force-field microscopy with optically levitated microspheres, *Phys. Rev. A* **99**, 023816 (2019).
- [32] F. Monteiro, W. Li, G. Afek, C.-L. Li, M. Mossman, and D. C. Moore, Force and acceleration sensing with optically levitated nanogram masses at microkelvin temperatures, *Phys. Rev. A* **101**, 053835 (2020).
- [33] Y. Arita, G. D. Bruce, E. M. Wright, S. H. Simpson, P. Zemánek, and K. Dholakia, All-optical sub-Kelvin sympathetic cooling of a levitated microsphere in vacuum, *Optica* **9**, 1000 (2022).
- [34] M. Rademacher, J. Millen, and Y. L. Li, Quantum sensing with nanoparticles for gravimetry: When bigger is better, *Adv. Opt. Technol.* **9**, 227 (2020).
- [35] A. Kawasaki, A. Fieguth, N. Priel, C. P. Blakemore, D. Martin, and G. Gratta, High sensitivity, levitated microsphere apparatus for short-distance force measurements, *Rev. Sci. Instrum.* **91**, 083201 (2020).
- [36] F. Monteiro, G. Afek, D. Carney, G. Krnjaic, J. Wang, and D. C. Moore, Search for Composite Dark Matter with Optically Levitated Sensors, *Phys. Rev. Lett.* **125**, 181102 (2020).

- [37] G. Afek, F. Monteiro, J. Wang, B. Siegel, S. Ghosh, and D. C. Moore, Limits on the abundance of millicharged particles bound to matter, *Phys. Rev. D* **104**, 012004 (2021).
- [38] C. P. Blakemore, A. Fieguth, A. Kawasaki, N. Priel, D. Martin, A. D. Rider, Q. Wang, and G. Gratta, Search for non-Newtonian interactions at micrometer scale with a levitated test mass, *Phys. Rev. D* **104**, L061101 (2021).
- [39] D. C. Moore and A. A. Geraci, Searching for new physics using optically levitated sensors, *Quantum Sci. Technol.* **6**, 014008 (2021).
- [40] G. Afek, D. Carney, and D. C. Moore, Coherent Scattering of Low Mass Dark Matter from Optically Trapped Sensors, *Phys. Rev. Lett.* **128**, 101301 (2022).
- [41] N. Priel, A. Fieguth, C. P. Blakemore, E. Hough, A. Kawasaki, D. Martin, G. Venugopalan, and G. Gratta, Dipole moment background measurement and suppression for levitated charge sensors, *Sci. Adv.* **8**, eab02361 (2022).
- [42] D. Carney, K. G. Leach, and D. C. Moore, Searches for massive neutrinos with mechanical quantum sensors, *PRX Quantum* **4**, 010315 (2023).
- [43] J. Millen, P. Z. G. Fonseca, T. Mavrogordatos, T. S. Monteiro, and P. F. Barker, Cavity Cooling a Single Charged Levitated Nanosphere, *Phys. Rev. Lett.* **114**, 123602 (2015).
- [44] G. P. Conangla, R. A. Rica, and R. Quidant, Extending Vacuum Trapping to Absorbing Objects with Hybrid Paul-Optical Traps, *Nano Lett.* **20**, 6018 (2020).
- [45] L. Dania, D. S. Bykov, M. Knoll, P. Mestres, and T. E. Northup, Optical and electrical feedback cooling of a silica nanoparticle levitated in a paul trap, *Phys. Rev. Res.* **3**, 013018 (2021).
- [46] T. Weiss, M. Roda-Llordes, E. Torrontegui, M. Aspelmeyer, and O. Romero-Isart, Large Quantum Delocalization of a Levitated Nanoparticle Using Optimal Control: Applications for Force Sensing and Entangling via Weak Forces, *Phys. Rev. Lett.* **127**, 023601 (2021).
- [47] M. Roda-Llordes, A. Riera-Campeny, D. Candoli, P. T. Grochowski, and O. Romero-Isart, Macroscopic quantum superpositions in a wide double-well potential, *arXiv:2303.07959*.
- [48] O. Romero-Isart, A. C. Pflanzer, F. Blaser, R. Kaltenbaek, N. Kiesel, M. Aspelmeyer, and J. I. Cirac, Large Quantum Superpositions and Interference of Massive Nanometer-Sized Objects, *Phys. Rev. Lett.* **107**, 020405 (2011).
- [49] O. Romero-Isart, Quantum superposition of massive objects and collapse models, *Phys. Rev. A* **84**, 052121 (2011).
- [50] J. Bateman, S. Nimmrichter, K. Hornberger, and H. Ulbricht, Near-field interferometry of a free-falling nanoparticle from a point-like source, *Nat. Commun.* **5**, 4788 (2014).
- [51] C. Wan, M. Scala, G. W. Morley, A. A. Rahman, H. Ulbricht, J. Bateman, P. F. Barker, S. Bose, and M. S. Kim, Free Nano-Object Ramsey Interferometry for Large Quantum Superpositions, *Phys. Rev. Lett.* **117**, 143003 (2016).
- [52] L. Neumeier, M. A. Ciampini, O. Romero-Isart, M. Aspelmeyer, and N. Kiesel, Fast quantum interference of a nanoparticle via optical potential control, *arXiv:2207.12539*.
- [53] O. Romero-Isart, L. Clemente, C. Navau, A. Sanchez, and J. I. Cirac, Quantum Magnetomechanics with Levitating Superconducting Microspheres, *Phys. Rev. Lett.* **109**, 147205 (2012).
- [54] O. Romero-Isart, Coherent inflation for large quantum superpositions of levitated microspheres, *New J. Phys.* **19**, 123029 (2017).
- [55] H. Pino, J. Prat-Camps, K. Sinha, B. P. Venkatesh, and O. Romero-Isart, On-chip quantum interference of a superconducting microsphere, *Quantum Sci. Technol.* **3**, 025001 (2018).
- [56] J. Hofer, G. Higgins, H. Huebl, O. F. Kieler, R. Kleiner, D. Koelle, P. Schmidt, J. A. Slater, M. Trupke, K. Uhl, T. Weimann, W. Wieczorek, F. Wulschner, and M. Aspelmeyer, High-Q Magnetic Levitation and Control of Superconducting Microspheres at Millikelvin Temperatures, *Phys. Rev. Lett.* **131**, 043603 (2023).
- [57] M. G. Latorre, G. Higgins, A. Paradkar, T. Bauch, and W. Wieczorek, Superconducting Microsphere Magnetically Levitated in an Anharmonic Potential with Integrated Magnetic Readout, *Phys. Rev. Appl.* **19**, 054047 (2023).
- [58] P. Maurer, C. Gonzalez-Ballester, and O. Romero-Isart, Quantum electrodynamics with a nonmoving dielectric sphere: Quantizing Lorenz-Mie scattering, *arXiv:2106.07975*.
- [59] R. J. Glauber and M. Lewenstein, Quantum optics of dielectric media, *Phys. Rev. A* **43**, 467 (1991).
- [60] Y. Arita, M. Mazilu, and K. Dholakia, Laser-induced rotation and cooling of a trapped microgyroscope in vacuum, *Nat. Commun.* **4**, 2374 (2013).
- [61] S. Kuhn, P. Asenbaum, A. Kosloff, M. Sclafani, B. A. Stickler, S. Nimmrichter, K. Hornberger, O. Cheshnovsky, F. Patolsky, and M. Arndt, Cavity-assisted manipulation of freely rotating silicon nanorods in high vacuum, *Nano Lett.* **15**, 5604 (2015).
- [62] T. M. Hoang, Y. Ma, J. Ahn, J. Bang, F. Robicheaux, Z.-Q. Yin, and T. Li, Torsional Optomechanics of a Levitated Nonspherical Nanoparticle, *Phys. Rev. Lett.* **117**, 123604 (2016).
- [63] S. Kuhn, A. Kosloff, B. A. Stickler, F. Patolsky, K. Hornberger, M. Arndt, and J. Millen, Full rotational control of levitated silicon nanorods, *Optica* **4**, 356 (2017).
- [64] S. Kuhn, B. A. Stickler, A. Kosloff, F. Patolsky, K. Hornberger, M. Arndt, and J. Millen, Optically driven ultra-stable nanomechanical rotor, *Nat. Commun.* **8**, 1670 (2017).
- [65] F. Monteiro, S. Ghosh, E. C. van Assendelft, and D. C. Moore, Optical rotation of levitated spheres in high vacuum, *Phys. Rev. A* **97**, 051802(R) (2018).
- [66] M. Rashid, M. Toroš, A. Setter, and H. Ulbricht, Precession Motion in Levitated Optomechanics, *Phys. Rev. Lett.* **121**, 253601 (2018).
- [67] J. Ahn, Z. Xu, J. Bang, Y.-H. Deng, T. M. Hoang, Q. Han, R.-M. Ma, and T. Li, Optically Levitated Nanodumbbell Torsion Balance and GHz Nanomechanical Rotor, *Phys. Rev. Lett.* **121**, 033603 (2018).
- [68] J. Ahn, Z. Xu, J. Bang, P. Ju, X. Gao, and T. Li, Ultrasensitive torque detection with an optically levitated nanorotor, *Nat. Nanotechnol.* **15**, 89 (2020).
- [69] F. van der Laan, R. Reimann, A. Militaru, F. Tebbenjohanns, D. Windey, M. Frimmer, and L. Novotny, Optically levitated rotor at its thermal limit of frequency stability, *Phys. Rev. A* **102**, 013505 (2020).
- [70] A. Pontin, H. Fu, M. Toroš, T. S. Monteiro, and P. F. Barker, Simultaneous cooling of all six degrees of freedom of an

- optically levitated nanoparticle by elliptic coherent scattering, *Nat. Phys.* **19**, 1003 (2023).
- [71] J. D. Jackson, *Classical Electrodynamics*, 3rd ed. (Wiley, New York, 1999).
- [72] L. Novotny and B. Hecht, *Principles of Nano-Optics*, 2nd ed. (Cambridge University Press, Cambridge, 2012).
- [73] A. A. R. Neves and C. L. Cesar, Analytical calculation of optical forces on spherical particles in optical tweezers: Tutorial, *J. Opt. Soc. Am. B* **36**, 1525 (2019).
- [74] J. E. Sipe and M. J. Steel, A Hamiltonian treatment of stimulated Brillouin scattering in nanoscale integrated waveguides, *New J. Phys.* **18**, 045004 (2016).
- [75] H. Zoubi and K. Hammerer, Optomechanical multimode Hamiltonian for nanophotonic waveguides, *Phys. Rev. A* **94**, 053827 (2016).
- [76] C. Cohen-Tannoudji, J. Dupont-Roc, and G. Grynberg, *Atom-Photon Interactions: Basic Processes and Applications* (Wiley, New York, 1998).
- [77] V. Jain, J. Gieseler, C. Moritz, C. Dellago, R. Quidant, and L. Novotny, Direct Measurement of Photon Recoil from a Levitated Nanoparticle, *Phys. Rev. Lett.* **116**, 243601 (2016).
- [78] D. Windey, C. Gonzalez-Ballester, P. Maurer, L. Novotny, O. Romero-Isart, and R. Reimann, Cavity-Based 3D Cooling of a Levitated Nanoparticle via Coherent Scattering, *Phys. Rev. Lett.* **122**, 123601 (2019).
- [79] U. Delić, M. Reisenbauer, D. Grass, N. Kiesel, V. Vučetić, and M. Aspelmeyer, Cavity Cooling of a Levitated Nanosphere by Coherent Scattering, *Phys. Rev. Lett.* **122**, 123602 (2019).
- [80] S. A. Beresnev, V. G. Chernyak, and G. A. Fomyagin, Motion of a spherical particle in a rarefied gas. Part 2. Drag and thermal polarization, *J. Fluid Mech.* **219**, 405 (1990).
- [81] I. H. Malitson, Interspecimen comparison of the refractive index of fused silica, *J. Opt. Soc. Am.* **55**, 1205 (1965).
- [82] *Handbook of Optics: Devices, Measurements, and Properties*, 2nd ed., edited by M. Bass, E. W. Van Stryland, D. R. Williams, and W. L. Wolfe (McGraw-Hill, New York, 2001), Vol. 2.
- [83] E. Joos and H. D. Zeh, The emergence of classical properties through interaction with the environment, *Z. Phys. B* **59**, 223 (1985).
- [84] M. A. Schlosshauer, *Decoherence and the Quantum-To-Classical Transition* (Springer, Berlin, 2007).
- [85] J. P. Gordon and A. Ashkin, Motion of atoms in a radiation trap, *Phys. Rev. A* **21**, 1606 (1980).
- [86] D. Hümmer, R. Lampert, K. Kustura, P. Maurer, C. Gonzalez-Ballester, and O. Romero-Isart, Acoustic and optical properties of a fast-spinning dielectric nanoparticle, *Phys. Rev. B* **101**, 205416 (2020).
- [87] C. Gonzalez-Ballester, J. Gieseler, and O. Romero-Isart, Quantum Acoustomechanics with a Micromagnet, *Phys. Rev. Lett.* **124**, 093602 (2020).
- [88] C. Gonzalez-Ballester, D. Hümmer, J. Gieseler, and O. Romero-Isart, Theory of quantum acoustomagnonics and acoustomechanics with a micromagnet, *Phys. Rev. B* **101**, 125404 (2020).
- [89] C. Henkel and R. Folman, Internal decoherence in nano-object interferometry due to phonons, *AVS Quantum Sci.* **4**, 025602 (2022).
- [90] X. Zambrana-Puyalto, D. D'Ambrosio, and G. Gagliardi, Excitation mechanisms of whispering gallery modes with direct light scattering, *Laser Photon. Rev.* **15**, 2000528 (2021).
- [91] S. Lepeshov, N. Meyer, P. Maurer, O. Romero-Isart, and R. Quidant, Levitated Optomechanics with Meta-Atoms, *Phys. Rev. Lett.* **130**, 233601 (2023).
- [92] V. Svák, J. Flajšmanová, L. Chvátal, M. Šiler, A. Jonáš, J. Ježek, S. H. Simpson, P. Zemánek, and O. Brzobohatý, Stochastic dynamics of optically bound matter levitated in vacuum, *Optica* **8**, 220 (2021).
- [93] J. Rieser, M. A. Ciampini, H. Rudolph, N. Kiesel, K. Hornberger, B. A. Stickler, M. Aspelmeyer, and U. Delić, Tunable light-induced dipole-dipole interaction between optically levitated nanoparticles, *Science* **377**, 987 (2022).
- [94] J. Vijayan, Z. Zhang, J. Piotrowski, D. Windey, F. van der Laan, M. Frimmer, and L. Novotny, Scalable all-optical cold damping of levitated nanoparticles, *Nat. Nanotechnol.* **18**, 49 (2023).
- [95] J. Hüpfel, N. Bachelard, M. Kaczvinszki, M. Horodynski, M. Kühmayer, and S. Rotter, Optimal Cooling of Multiple Levitated Particles through Far-Field Wavefront Shaping, *Phys. Rev. Lett.* **130**, 083203 (2023).
- [96] A. Ranfagni, P. Vezio, M. Calamai, A. Chowdhury, F. Marino, and F. Marin, Vectorial polaritons in the quantum motion of a levitated nanosphere, *Nat. Phys.* **17**, 1120 (2021).
- [97] A. de los Ríos Sommer, N. Meyer, and R. Quidant, Strong optomechanical coupling at room temperature by coherent scattering, *Nat. Commun.* **12**, 276 (2021).
- [98] C. Gonzalez-Ballester, J. A. Zielińska, M. Rossi, A. Militaru, M. Frimmer, L. Novotny, P. Maurer, and O. Romero-Isart, Suppressing Recoil Heating in Levitated Optomechanics Using Squeezed Light, *PRX Quantum* **4**, 030331 (2023).
- [99] E. L. Hill, The theory of vector spherical harmonics, *Am. J. Phys.* **22**, 211 (1954).
- [100] C. F. Bohren and D. R. Huffman, *Absorption and Scattering of Light by Small Particles* (Wiley, New York, 1998).
- [101] B. Richards, E. Wolf, and D. Gabor, Electromagnetic diffraction in optical systems, II. Structure of the image field in an aplanatic system, *Proc. R. Soc. A* **253**, 358 (1959).